Robust Acoustic Signal Detection and Synchronization in a Time Varying Ocean Environment
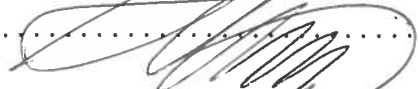
by

Ryan Thomas Gieleghem

BSEE, University of South Florida (2005)

Submitted to the Department of Mechanical Engineering
& Department of Applied Ocean Science and Engineering
in partial fulfillment of the requirements for the degree of

Master of Science

at the

MASSACHUSETTS INSTITUTE OF TECHNOLOGY

and the

WOODS HOLE OCEANOGRAPHIC INSTITUTION

September 2012

Author . . . .
Department of Mechanical Engineering
& Department of Applied Ocean Science and Engineering
August 2, 2012

Certified by . . . .
Dr. James C. Preisig
Associate Scientist with Tenure
Woods Hole Oceanographic Institution
Thesis Supervisor

Accepted by . . . .
Dr. Henrik Schmidt
Chair, Joint Committee for Applied Ocean Science and Engineering
Massachusetts Institute of Technology

Accepted by . . . .
Dr. David E. Hardt
Chair, Committee on Graduate Students - Mechanical Engineering
Massachusetts Institute of Technology

Robust Acoustic Signal Detection and Synchronization in a Time Varying Ocean Environment

by

Ryan Thomas Gieleghem

Submitted to the Department of Mechanical Engineering
& Department of Applied Ocean Science and Engineering
on August 2, 2012, in partial fulfillment of the
requirements for the degree of
Master of Science in Mechanical Engineering and
Applied Ocean Science and Engineering

Abstract

Signal detection and synchronization in the time varying ocean environment is a difficult endeavor. The current common methods include using a linear frequency modulated chirped pulse or maximal length sequence as a detection pulse, then match filtering to that signal. In higher signal to noise ratio (SNR) environments (~ 0 dB and higher) this has been a suitable solution. As the SNR drops lower however, this solution no longer provides an acceptable probability of detection for a given tolerable probability of false alarm. The issue derives from the inherent coherence issues in the ocean environment which limit the useful matched filter length. This thesis proposes an alternative method of detection based on a recursive least squares linearly adaptive equalizer which we term the Adaptive Linear Equalizer Detector (ALED). This detectors performance has demonstrated reliable probability of detection with minimal interfering false alarms with SNR as low as -20 dB. Additionally this thesis puts forth a computationally feasible method for implementing the detector.

Thesis Supervisor: Dr. James C. Preisig
Title: Associate Scientist with Tenure
Woods Hole Oceanographic Institution

Dedication

This Thesis is dedicated to my three beautiful daughters Kathryn, Klaire, and Khloe, who endured countless daddyless days and nights while I toiled away in my office struggling with one idea or another. To my unborn daughter Keira, thank you for not being too hard on mommy while I was away. And finally, to my beautiful wife Elizabeth, who has been waiting two years for me to say *the end*, I love you, and *we* did it.

Acknowledgments

First and foremost, I would like to thank Dr. Jim Preisig. Without his unending and undying patience for my relentless questions this thesis would have not come to fruition.

Many thanks to Atulya Yellepeddi and Milutin Pajovic, my cohorts in research, who both proved time and time again, you can teach an old dog new tricks.

To Scott and Marissa Haven - thank you for being my family away from home. All of the dinner invitations made for a wonderful distraction.

Additionally I would like to thank Captain David Roberts (USN) and Commander Gorge Arnold (USN). They not only helped mentor me into the man I have become, but perhaps saw in me what I did not see in myself, and guided me into applying for the Joint Program.

And finally I would like to thank the United States Navy, the Oceanographer of the Navy, and the Naval Post-Graduate School for the opportunity to participate in this program.

Contents

List of Figures

Chapter 1

Introduction

The sea has never been friendly to man. At most it has been the accomplice of human restlessness

-Joseph Conrad

1.1 Motivation

Signal communications in the ocean environment is a challenging endeavor. We are often looking to communicate between distant ships or even a system of moored buoys sparsely placed in the ocean. Transmission losses increase rapidly as signal frequency rises due to chemical relaxation in addition to volumetric spreading losses (Jensen et al., 2011). This relegates transmission frequencies down to a few tens of kilohertz for ranges of any significance, reducing the available bandwidth (Stojanovic, 1996).

Additionally the ocean presents a multipath environment. The surface, bottom and objects in between the source and receiver set up multiple reflection points. In addition, sound refraction due to the spatial variability of sound speed bends sound rays into different paths (Stojanovic and Preisig, 2009).

To further complicate things, the channel exhibits time variability. From surface waves changing the reflection boundaries to transmitter and receiver motion inducing frequency shifting and spreading, the end result is channel that varies on a short enough time scale to affect the signal (Stojanovic and Preisig, 2009).

Even in this, most unruly of environments, it is important to work towards a robust communications system capable of handling mother nature's challenges. However, every conversation must begin with a *hello*, every greeting a *handshake* and it is in this realm where this thesis will takes it aim: acoustic signal detection.

Currently in the literature there are two main forms of signal detectors: Matched Filter (MF) detectors and Energy Detectors (ED). The MF detector is the optimum detector in additive white Gaussian noise (AGWN) when the transmitted signal is known (North, 1963). While the ED implements a generalized likelihood ratio test (GLRT) for the detection of unknown deterministic signals in white Gaussian noise (Kay, 1998).

We will briefly explore the ED as it could be utilized to detect the presence of an unknown transmission. If we wish our transmissions to be undetectable by receivers other than our intended recipient, an ED analysis sheds light on the limit on transmit signal power that can be used without reliable detection by an unintended recipient.

The MF detector is the most commonly used detector when the transmitted signal is known. In a communication scheme, the MF detector is used for synchronization of an incoming data signal. It can flag an incoming section of data for further processing and decoding. This will be the basis for which we compare the new detector proposed in this thesis.

1.1.1   Energy Detection Background

In Harry Urkowitz's paper (Urkowitz, 1967) on the energy detection of unknown deterministic signals he demonstrates that when the form of the signal is unknown and the noise is zero mean and Gaussian the ED is the appropriate method of detection. In his paper however, he assumes the spectral location of the signal and its duration are known. An ED with this information provides an upper bound on performance for any energy detection scheme with less signal knowledge.

Others have attempted to develop detectors that can overcome a lack of spectral or signal duration knowledge. For instance, if the signal is of unknown length, it has been proposed that using multiple energy detectors (MED), each with a layered

signal length estimate (N, N/2, N/4, ... ,N/L), where N is the estimated signal length and L is the number of layers, can provide reasonable performance when compared to the standard ED where the length is known (Vergara et al., 2010). However, the optimum performance for this detector occurs when the number of layers is equal to one and the estimated signal duration is the actual duration. As the signal length estimate and actual signal duration mismatch increases the performance degrades. In addition the MED chooses detection when any one of the layers indicates a signal is present, therefore the false alarm probability rises as the number of layers increases.

Vegara *et al.* further proposes a similar layered approach via frequency transforms to detect signals with unknown spectra (Vergara et al., 2010). However, again we see that the performance of this detector is upper bounded by the clairvoyant detector that has perfect knowledge of time duration and signal bandwidth.

The ED is only the optimum detector when both the signal and the noise are white Gaussian zero mean random processes (Kay, 1998). In cases when the unknown signal deviates from this specification the ED is often a good computationally feasible solution. However this opens up the door to better solutions. Signal detection by convolving a finite portion of the received signal with itself has been proposed on the premise that for a noise random variable that is independent and identically distributed the convolution operator has a much lower noise output than that of the auto-correlation output at zero shift given by the standard ED (Chan et al., 2006). However, Y.T. Chan *et al.* demonstrated that while the output of the ED is independent of pulse shape, the Convolution Detector (CD) is highly dependent on signal shape and only achieved notable gains for signals with nonzero means. Furthermore significant gains were only seen signal to noise ratios (SNR) of greater than -10 dB.

1.1.2   Matched Filter Background

In the conventional MF detector, for a signal in additive white Gaussian noise, we convolve the received signal, containing the data signal plus noise, with the time reversed data signal. This method maximizes the SNR at the output of the filter

(North, 1963). However we often only know the form of the transmitted signal. If the channel impulse response is anything other than the delta function the MF detector is no longer optimal. In the ocean environment, time dispersion and multipath channel effects cause energy spreading that reduces the gain of the conventional matched filter.

The optimal MF detector would now be the time reversed version of the data signal convolved with the channel. However this would require knowing the channel exactly. Hermand and Roderick propose a method called Model Based Matched Filtering (MBMF), where the received signal is filtered with the time reversed version of the transmitted signal convolved with a channel model (Hermand and Roderick, 1993). Their model is based on knowledge of the sound velocity profile, historical bottom loss, depth of the source and receiver and the range between them. With this knowledge, Hermand and Roderick demonstrated that the MBMF outperformed the conventional MF.

In other cases, the noise may not be white. Here the optimal detector first whitens the noise, then applies a filter that is matched to the data signal distorted by the whitening filter (Turin, 1960). However to accomplish this task the noise covariance matrix must be known. Reed *et al.* suggest methods for estimating the noise covariance matrix and Kelly derives a threshold for a detector based on this estimate, but both require a secondary receiver input that is based on noise alone (Reed et al., 1974) (Kelly, 1986). In a radar system where the transmitter and receivers are co-located it is possible to obtain signal free noise data, but in a point to point communications scheme at any point in time the received signal may or may not contain the transmitted signal so reliably identifying signal free receptions of the noise can be problematic.

In communication schemes MF detectors are used to synchronize incoming data streams prior to equalization and decoding. Often linear frequency modulated (LFM) chirps or Maximum Length Sequences (MLS), also known as m-sequences, are used for their sharp peaks at the output of a matched filter denoting signal arrival. If the transmitter/receiver pair are not maintaining a fixed distance some Doppler effect will be introduced. While LFM chirps are more Doppler tolerant than m-sequences,

the conventional method for handing this situation is employing a bank of matched filters that covers the Doppler span (Remley, 1966). See Chapter 3 of this thesis for a full discussion on how Doppler effects LFM pulses and m-sequences. Feng Wie *et al* propose an alternative method that utilizes a hyperbolic frequency modulated (HFM) signal (Wei et al., 2010). Their method utilizes three HFM pulses, an initial "wake up" pulse, where the output of a MF detector is compared with a threshold, followed by two pulses, an "up" and a "down" pulse, who's relative peak spacing is utilized to measure the Doppler.

1.1.3 Adaptive Equalization for Detection

This thesis demonstrates the use of a linear adaptive equalizer for detection. As the detector receives "good data" or data containing a transmitted signal, it estimates what the received bit should be and compares that to the known transmitted bit. The bit error rate (BER) is tracked, and when it falls below a predetermined threshold it assumes detection is achieved.

This thesis will further demonstrate that a detector of this form is desirable because the decision threshold level set in the detector is only dependent on SNR and not absolute signal levels whereas in a MF detector the value of the decision threshold is a function of the ambient noise level. As the ambient noise level rises the threshold must be reset to prevent spurious false alarms. In the adaptive equalizer detector, the threshold is a function of the BER. This allows a decision threshold to be set independently of received signal level and therefore does not require consistent readjusting by the operator.

1.2 Objectives

1. Propose a computationally feasible method of linear adaptive equalization for signal detection and synchronization.

2. Demonstrate the effectiveness of linear adaptive equalization when compared

to the matched filter and energy detectors in very low signal to noise ratio environments.

3. Determine a reasonable set of real world operating characteristics for signal detection in a broad range of underwater acoustic conditions.

1.3 Notation

Bold uppercase letters will be used to denote matrices and bold lower case letters will denote vectors. Unless otherwise specified all vectors will be column vectors. The superscripts T, *, and H will denote transpose, conjugate, and Hermitian (complex conjugate transpose) respectively. Upper and lower case normal weight variables represent real, imaginary and complex valued scalars. Additionally, unless otherwise noted, all signals are assumed to have already been sampled. See Table 1.1 for clarification and additional notations.

Symbol Type	Meaning
$\mathbf{A}$ (boldface, uppercase symbol)	Matrix
$\mathbf{x}$ (boldface, lowercase symbol)	Column vector (size inferred from context)
x (non-boldface math symbol)	Scalar constant or variable
$x[n]$	Discrete-time Signal at sample n
$*$	Complex Conjugate
T	Matrix Transpose
H	Matrix Hermitian
$E[\bullet]$	Expectation
$var(\bullet)$	Variance
$\mid \bullet \mid$	Determinant
$\parallel \bullet \parallel$	L2 Norm
$\mathcal{N}(\mu, \sigma)$	Normal PDF w/ mean $= \mu$, variance $= \sigma^2$
$\mathcal{CN}(\mu, \sigma)$	Complex Normal PDF w/ mean $= \mu$, variance $= \sigma^2$

Table 1.1: Notations

1.4   Organization

Chapter 2 will provide an analysis of the energy detector. Chapter 3 will present the matched filter derivation. This will form the basis for comparison with linear adaptive equalization detection. Chapter 4 will provide the structure of the linear adaptive equalizer detector. Chapter 5 will discuss the real world experiment used to test the detectors in July of 2011. Chapter 6 will compare the results of each detector. Finally, Chapter 7 will discuss conclusions and areas for future research.

Chapter 2

Energy Detection

2.1 Introduction

This thesis aims to proffer a new acoustic communications detection scheme that outperforms current methods in the ocean environment. However if we were simply concerned with signal detection for a given range it seems we could simply ensonify the ocean with larger amounts of energy until our desired probability of detection is reached. Neglecting the potential impact to marine life, this has the additional drawback of notifying any nearby hydrophone of the transducer's presence. If the purpose of the communications are for covert operations the sender may receive unwanted attention from an adversary.

This chapter develops the potential signal detection method our opponent may utilize to detect our signals. Section 2.2 delineates the signal model used in the remainder of the chapter. Section 2.3 introduces the form of the energy detector and derives the expected performance based on the statistics of our signal model. Finally, Sections 2.4 and 2.5 introduce receiver operating characteristic curves and a useful method for comparing these curves.

2.2 Signal Model

The generic signal detection problem we encounter in ocean acoustics is determining whether or not a transmitted signal $s[n]$ is contained in the received signal $x[n]$.

$$x[n] = w[n] \qquad \text{No Signal Present}$$
$$x[n] = s[n] + w[n] \qquad \text{Signal Present} \qquad (2.1)$$

Here, $w[n]$ has been assumed to be a wide sense stationary (WSS) random process. Furthermore we will assume that $w[n]$ is additive white complex Gaussian noise (AWCGN) with zero mean and variance σ_w^2, is independent at each time step and independent of the signal. The signal $s[n]$ is an unknown complex random signal with zero mean and variance σ_s^2.

2.3 The Detector

With so little known about the transmitted signal it seems reasonable that one method for determining whether or not a signal is present is to check the energy level in the received vector. One would expect that the energy level will increase when the data signal is present when compared to noise alone.

Here we will make our first assumptions about the signal, its signal duration and the bandwidth it occupies are known. Knowing the signal duration allows the ED to make maximal use of the signal without adding any additional noise. Knowing the bandwidth of the signal allows for improvement in the signal to noise ratio by first removing noise outside of the signal's spectrum. These are the same two assumptions made by Urkowitz in his paper on the detection of unknown signals in which he demonstrates the effectiveness of ED on unknown signals (Urkowitz, 1967).

Chapter 1 of this thesis discusses Vegara's paper (Vergara et al., 2010) proposing multiple energy detectors for signals with unknown duration, but it is intuitive that knowing the signal duration will place an upper bound on any detector that is deprived

of this information. A similar statement holds true for unknown signal spectra. Kay proposes a solution using an auto-regressive process that performs better than the ED when the signal spectra in unknown, however it is still bounded by the clairvoyant ED (Kay, 1985).

The Neyman-Pearson structure of the energy detector implements the following test (Kay, 1998):

$$T = \sum_{n=0}^{N-1} x[n]^* x[n] \underset{'H_0'}{\overset{'H_1'}{\underset{<}{\gtrless}}} \gamma \tag{2.2}$$

where H_0 and H_1 represents our two hypothesizes of the received vector containing noise only or noise with signal present, N is the signal duration length, and γ is the threshold that we will use to determine which hypothesis is true.

At each time step n, for $n = 0, 1, \ldots, N-1$, $x[n]$ is an independent identically distributed (IID) Gaussian random variable. If $x[n] \sim \mathcal{CN}(0, 1)$ the test statistic is the sum of squared IID random variables which corresponds to a chi-squared (χ^2_{2N}) distribution with $2N$ degrees of freedom (Papoulis and Pillai, 2002). An equivalent test statistic is:

$$T' = \frac{1}{N} \sum_{n=0}^{N-1} |x[n]|^2 \tag{2.3}$$

The new test statistic can thought of as an estimate of the variance where $\sigma_x^2 = \sigma_w^2$ under H_0 and $\sigma_x^2 = \sigma_s^2 + \sigma_w^2$ under H_1 (Kay, 1998). For large values of N and using the independence of each x, we can apply the central limit theorem to our new test statistic and approximate it as a Gaussian random variable. As with all Gaussian random variables, it is fully described by its first two moments. Solving for the first two moments yields:

$$E[T'] = \frac{1}{N} \sum_{n=0}^{N-1} E[|x[n]|^2] = \sigma_x^2 \tag{2.4}$$

$$var(T') = \frac{1}{N^2} \sum_{n=0}^{N-1} var(|x[n]|^2) = \frac{1}{N}(\sigma_x^2)^2 \tag{2.5}$$

Therefore under H_0 the test statistic T' is $\sim \mathcal{N}(\sigma_w^2, \frac{1}{N}\sigma_w^4)$ and under H_1 the test statistic T' is $\sim \mathcal{N}(\sigma_s^2 + \sigma_w^2, \frac{1}{N}(\sigma_s^2 + \sigma_w^2)^2)$.

2.4   Receiver Operating Characteristic

Since this thesis will evaluate several signal detectors of different forms it is useful here to introduce the metric by which they will be compared. We denote the probability of false alarm (P_{FA}) as the probability of saying a signal detection has occurred when no signal is present or more formally $P_{FA} = P(`H_1`|H_0)$. Furthermore we denote the probability of detection as $P_D = P(`H_1`|H_1)$.

The Receiver Operating Characteristic (ROC) curve is a plot of P_D versus P_{FA} as a function of threshold or other detector setting. The curve, for example, allows you to compare trade-offs between allowing a higher P_{FA} to the improvement in P_D. Additionally it allows you to evaluate changes in P_D, for a given P_{FA} due to manipulating the detector settings. Finally, since the ROC curve is only a function of the receiver detection and false alarm probabilities that used to generated it, it allows for meaningful comparisons between different types of detectors.

To calculate the ROC we first need the probability distributions of the test statistic under each hypothesis. These were given in the previous section for large N as approximately Gaussian. Normalizing $\sigma_w^2 = 1$ and noting $\frac{\sigma_s^2}{\sigma_w^2} = SNR$ reduces the probability density functions to:

$$H_0 : f_{T|H}(t|H_0) = \mathcal{N}(1, \frac{1}{N})$$
$$H_1 : f_{T|H}(t|H_1) = \mathcal{N}(1 + SNR, \frac{1}{N}(1 + SNR)^2). \tag{2.6}$$

To calculate P_D and P_{FA} we simply integrate the appropriate probability density functions for each value of γ from γ to ∞. P_D and P_{FA} are given by:

$$P_{FA} = \int_{\gamma}^{\infty} f_{T|H}(t|H_0)dt$$
$$P_D = \int_{\gamma}^{\infty} f_{T|H}(t|H_1)dt. \tag{2.7}$$

A sample ROC for an energy detector of length $N = 127$ is provided in Figure 2-1 for multiple SNR levels. The value $N = 127$ was chosen because it is the length of a maximal length sequence used later in the thesis. From (2.6) we can see the variance of the test statistic is inversely proportional to the length of the energy detector, therefore increasing the length of the signal transmission and the corresponding detection filter will result in improved receiver performance. Figure 2-2 demonstrates the filter length relationship at -20 dB SNR.
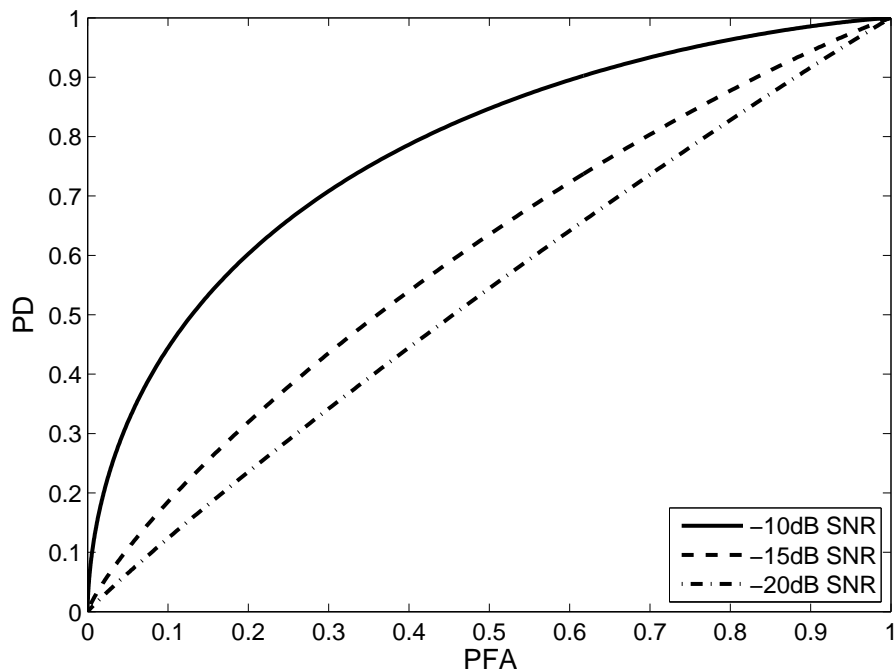
Figure 2-1: Theoretical Energy Detector ROC for N = 127 at -10, -15 and -20 dB SNR

2.5 ROC Area

A useful measurement when comparing ROCs is the area under the curve. In the ideal situation, there exists perfect detection with no false alarms. In this case, the ROC curve would immediately go to one and stay there for all threshold values. It is easy to calculate that the area under this ROC curve is equal to one, which sets the upper bound. The diagonal line on the ROC is achieved for equal probabilities of detection and false alarm at all threshold values, this is equivalent to the detector guessing by flipping a fair coin. If the ROC fell below this diagonal line, the corrective action would be to flip the detector decision and the ROC curve would mirror itself back above the diagonal. Therefore the lower bound is set by the diagonal line which has an area of $\frac{1}{2}$. So each ROC area will fall in the set $[\frac{1}{2}, 1]$, and the design goal for a signal detector is to approach an area of 1.

Figure 2-2: Theoretical Energy Detector ROC for various N values at -20 dB SNR

Chapter 3

Matched Filter

3.1   Introduction

The matched filter has been well known in signal detection since Dwight North introduced the concept in his paper on signal/noise discrimination in pulsed-ca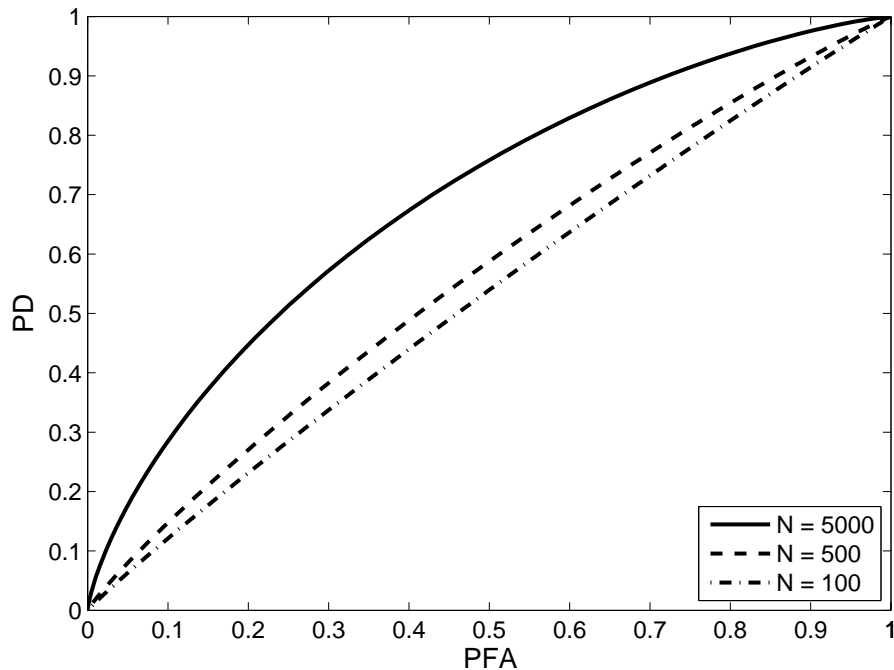rrier systems in 1943 (North, 1963). A complete treatise on matched filters is given by George Turin (Turin, 1960). This thesis will not attempt to recreate this work but rather provide a basic understanding of the matched filter. The derivation below will parallel George Turin's derivation (Turin, 1960). The matched filter detector will provide the basis comparison for all detectors described in the remaining chapters.

This chapter begins, in Section 3.2, by developing the optimal linear filter for signal detection in white Gaussian noise. In Section 3.3 we develop the optimal detector structure, develop the expected performance based on the statistics for this structure and generate ROCs. Section 3.4 changes the white noise assumption and looks at the effects. Section 3.5 investigates the optimum detector for a signal with unknown complex amplitude in complex Gaussian noise. Again we arrive at the matched filter, but this time followed by an envelope detector. Section 3.6 derives the expected performance for the maximum likelihood matched filter and generates the ROCs. Sections 3.7 to 3.10 develop the scattering function, ambiguity function and investigates how signal design and the channel properties can affect the performance of the matched filter.

3.2   Optimal Detection in White Gaussian Noise

The generic signal detection problem we encounter in ocean acoustics is determining whether or not a transmitted signal $s[n]$ is contained in the received signal $x[n]$.

$$x[n] = w[n]$$
$$x[n] = s[n] + w[n] \tag{3.1}$$

Here, $w[n]$ has been assumed to be a wide sense stationary (WSS) random process. For this initial derivation we will consider $w[n]$ is additive white Gaussian noise (AWGN) with zero-mean and variance σ_w^2. Further more we will assume we want use a linear filter to determine whether or not the signal is present. The output of the linear filter is the discrete time convolution of $x[n]$ and $h[n]$.

$$y[n] = \sum_{-\infty}^{\infty} x[k]h[n-k] \tag{3.2}$$

Due to the linearity of the filter we can break down the output of the filter into the sum of its signal and noise component by super position. Therefore

$$y[n] = y_s[n] + y_w[n] \tag{3.3}$$

Where y_s is the signal portion of the output and y_w is the noise portion of the output.

To determine if the signal is present at n_0 we would like to make the instantaneous power at n_0 as large as possible relative to the average noise power (Turin, 1960). The output noise Power Spectral Density (PSD) is given by (3.4). Where $H(e^{j\omega})$ is the discrete time Fourier transform of $h[n]$ and in the second equality we have used the fact that the noise is white.

$$S_{y_w y_w}(e^{j\omega}) = |H(e^{j\omega})|^2 S_{ww}(e^{j\omega}) = |H(e^{j\omega})|^2 \sigma_w^2 \tag{3.4}$$

Therefore the average noise power is given by (3.5).

$$\frac{\sigma_w^2}{2\pi} \int_{2\pi} |H(e^{j\omega})|^2 d\omega \tag{3.5}$$

Next we look at the signal energy. We start with the fact that the Fourier transform of $y_s[n]$ is the product of $S(e^{j\omega})$ and $H(e^{j\omega})$, Fourier transforms of $s[n]$ and $h[n]$ respectively. Now taking the inverse Fourier transform at $n = n_0$ yields

$$y_s[n_0] = \int_{2\pi} S(e^{j\omega}) H^*(e^{j\omega}) e^{j\omega n_0} \frac{d\omega}{2\pi} \tag{3.6}$$

Therefore in maximizing the instantaneous signal power to average noise power at $n = n_0$ we are trying to maximize the ratio of the square of (3.6) to (3.5). For convenience we will call this ratio ρ.

$$\rho = \frac{|\int_{2\pi} S(e^{j\omega}) H^*(e^{j\omega}) e^{j\omega n_0} \frac{d\omega}{2\pi}|^2}{\sigma_w^2 \int_{2\pi} |H(e^{j\omega})|^2 \frac{d\omega}{2\pi}} \tag{3.7}$$

Here it is useful to recall the Cauchy-Schwarz inequality. Where we see that taking the magnitude squared of the inner product of two functions is less than or equal to the product of the integrated squared functions.

$$\left| \int s(x)h(x)dx \right|^2 \leq \int |s(x)|^2 dx \int |h(x)|^2 dx \tag{3.8}$$

which reaches equality only when $h(x) = ks^*(x)$. Utilizing this fact we see that

$$\rho \leq \frac{1}{\sigma_w^2} \int_{2\pi} |S(e^{j\omega})|^2 d\omega \tag{3.9}$$

Noting that numerator in (3.9) is the total signal energy, we see that the ratio ρ equals the signal to noise ratio when $h[n] = ks^*[-n]$. Which is to say, ρ is maximized when the linear filter is *matched* to the signal.

3.3 The Optimal Detector

The following, or similar derivation, has been completed in numerous publications by (Oppenheim and Verhese, 2010),(Kay, 1998), and other authors. From the previous

section we saw that when using a linear filter that was matched to the signal we received a maximum output when the signal was present in the filter. From here, we wish to design a detector that will indicate whether the signal is present or not. We first propose the following binary hypothesis test

$$
\begin{aligned}
H_0 &: x[n] = w[n] \\
H_1 &: x[n] = \sqrt{\xi} s[n] + w[n]
\end{aligned}
\tag{3.10}
$$

Where x[n] is a finite length Discrete-Time (DT) random process of length N, ξ is the signal energy, $\sum_{n=1}^{N} s[n]^2 = 1$ and $s[n] = 0$ for $n < 0$ or $n \geq N$. For this simple example we will take $w[n]$ to be a random noise process such that $w[n]$ are independent zero mean Gaussian random variables with variance σ_w^2 for $n = 1, 2, 3, \ldots, N$.

We would like to determine if the signal is present with a minimum probability of error. To do this we start with the Maximum *A-Posteriori* Probability rule or the MAP rule:

$$
f(H_1 | x[1], x[2], \ldots, x[N]) \underset{`H_0\text{'}}{\overset{`H_1\text{'}}{\gtrless}} f(H_0 | x[1], x[2], \ldots, x[N]).
\tag{3.11}
$$

Here we apply apply Baye's rule to put the probabilities in terms of known quantities (Papoulis and Pillai, 2002).

$$
f(x[1], x[2], \ldots, x[N] | H_1) P(H_1) \underset{`H_0\text{'}}{\overset{`H_1\text{'}}{\gtrless}} f(x[1], x[2], \ldots, x[N] | H_0) P(H_0).
\tag{3.12}
$$

With $w[n]$ being both white and Gaussian, the respective conditional densities for H_0 and H_1 are given by: (Papoulis and Pillai, 2002)

$$f(x[1], x[2], \ldots, x[N]|H_0)P(H_0) = \frac{1}{(2\pi\sigma_w^2)^{L/2}} exp\left(-\sum_{n=1}^{N} \frac{(x[n])^2}{2\sigma_w^2} \right) \tag{3.13}$$

and

$$f(x[1], x[2], \ldots, x[N]|H_1)P(H_1) = \frac{1}{(2\pi\sigma_w^2)^{L/2}} exp\left(-\sum_{n=1}^{N} \frac{(x[n] - s[n])^2}{2\sigma_w^2} \right). \tag{3.14}$$

Placing (3.13) and (3.14) on either side of (3.12) with the *a priori* probabilities of H_0 and H_1 gives us the desired test. However, it is cumbersome to work with these distributions. To simplify this relation we apply a non-linear strictly increasing function to both sides (Papoulis and Pillai, 2002). Taking the natural logarithm of both sides of (3.12) and rearranging yields

$$\sum_{n=1}^{N} x[n]s[n] \underset{\underset{'H_0'}{<}}{\overset{\overset{'H_1'}{>}}{}} \sigma_w^2 \ln\left(\frac{P(H_0)}{P(H_1)} \right) + \frac{1}{2}\sum_{n=1}^{N} s^2[n] \tag{3.15}$$

From (3.15) we quickly see two things. First, our threshold for deciding which hypothesis is correct is set by the *a priori* probabilities, the signal energy, and the noise energy. Second, the left side of (3.15) is simply the output of the linear filter sampled at $n = 0$. This is pictorially shown in Figure 3-1.

In the case of acoustic signal detection, it is more likely than not that we will not have the requisite *a priori* probabilities. Therefore we will re-frame the problem in the Neyman-Pearson formulation.

In the Neyman-Pearson formulation we set the entire right side of (3.15) to γ. The threshold γ is a value we can choose based on our tolerance for false alarms and missed detections. We denote the probability of false alarm (P_{FA}) as the probability of saying a signal detection has occurred when no signal is present or more formally $P_{FA} = P(\text{'}H_1\text{'}|H_0)$. Furthermore we denote the probability of detection as $P_D = P(\text{'}H_1\text{'}|H_1)$.

Since $x[n]$ is a Gaussian random process then $g = \sum_{n=1}^{N} x[n]s[n]$ is a Gaussian random variable and it is easy to show

$$H_0 : E[g] = E\left[\sum_{n=1}^{N} x[n]s[n]\right] = E\left[\sum_{n=1}^{N} w[n]s[n]\right] = 0$$

$$H_1 : E[g] = E\left[\sum_{n=1}^{N} x[n]s[n]\right] = E\left[\sum_{n=1}^{N} \sqrt{\xi}s^2[n]\right] = \sqrt{\xi} \tag{3.16}$$

and

$$H_0 : var(g|H_0) = \sigma_w^2 \sum_{n=1}^{N} s^2[n]$$

$$H_1 : var(g|H_1) = \sigma_w^2 \sum_{n=1}^{N} s^2[n] \tag{3.17}$$

We see that under both hypotheses the probability density function of the output of the matched filter is normally distributed with different means and the same variance. Remembering that $\sum_{n=1}^{N} s^2[n] = 1$ we get the following:
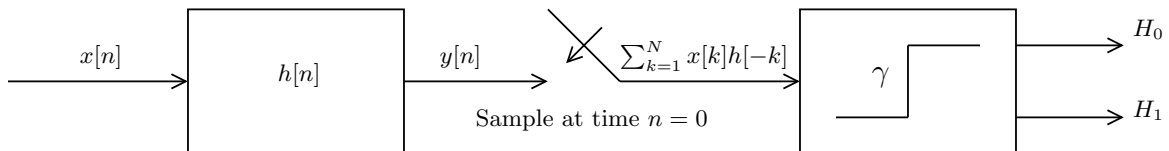
Figure 3-1: Linear Filter & Decision Device
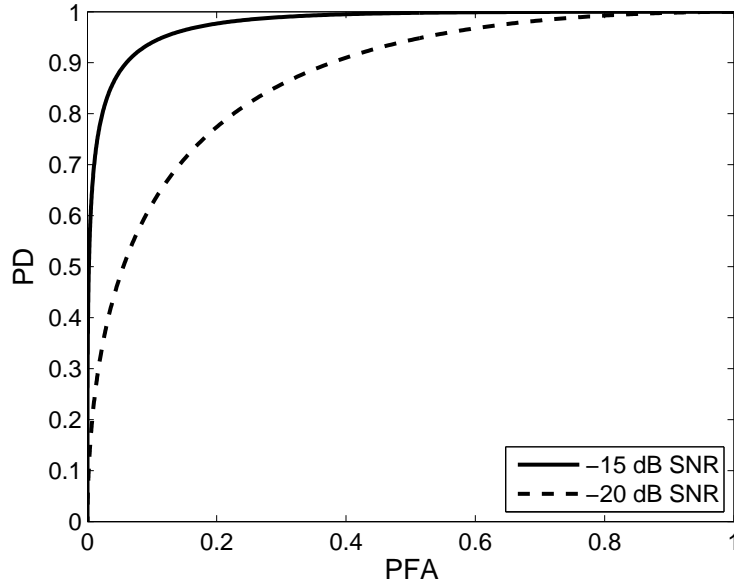
Figure 3-2: Theoretical ROC for a MF in AWGN, filter length $N = 127$

$$H_0 : f_{G|H}(g|H_0) = \mathcal{N}(0, \sigma_w^2)$$
$$H_1 : f_{G|H}(g|H_1) = \mathcal{N}(\sqrt{\xi}, \sigma_w^2). \tag{3.18}$$

From (3.18) we see that the difference in the two hypotheses probability density functions is merely a function of the signal energy. Given these two density functions we can calculate a Receiver Operating Characteristic (ROC) curve. The ROC is a plot of P_D versus P_{FA} for a given threshold γ. With (3.19) we can find P_D and P_{FA} for each γ. The ROC is shown in Figure 3-2.

$$P_{FA} = \int_{\gamma}^{\infty} f_{G|H}(g|H_0) dg$$
$$P_D = \int_{\gamma}^{\infty} f_{G|H}(g|H_1) dg \tag{3.19}$$

3.4 Colored Noise

In the case of colored noise we can still determine the optimum filter. One approach is to first whiten the noise and then apply a matched filter. Assume we have the same signal model as given by (3.10) only now the noise $v[n]$ is colored, rather than white, with autocorrelation function $R_{vv}[m]$ given by (3.20).

$$R_{vv}[m] = E[v[n+m]v[n]] = E[v[n]v[n-m]] \tag{3.20}$$

First we apply a whitening filter $h_w[n]$ to the received signal, whose Fourier transform is given by (3.21) (Oppenheim and Schafer, 2010).

$$\|H_w(e^{j\omega})\| = \sqrt{\frac{S_{ww}(e^{j\omega})}{S_{nn}(e^{j\omega})}} = \frac{1}{\sqrt{S_{nn}(e^{j\omega})}} \tag{3.21}$$

Here, it has been assumed that $S_{vv}(e^{j\omega})$ and $S_{ww}(e^{j\omega})$ are the power spectral densities of the colored and white noise respectively, and $\sigma_w^2 = 1$. The output of the whitening filter is now a new signal corrupted with white noise where the new signal is given by $g[n] = \sum_{l=-\infty}^{\infty} s[l]h_w[n-l]$. Section 3.2 demonstrated that the optimum detector for a signal in white noise is the matched filter, therefore we now match filter to the new signal, where $h_{MF} = kg^*[-n]$, for any non-zero scale value k. This yields an optimum filter for detection in colored noise of $h_{\mathrm{OPT}} = h_w[n] * h_{MF}[n]$ (Turin, 1960). This is shown pictorially in Figure 3-3.
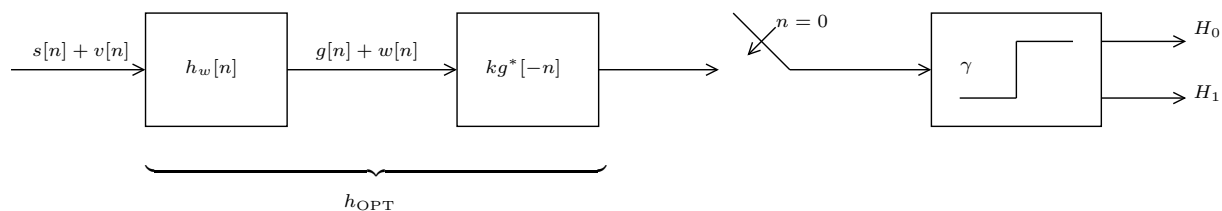

Figure 3-3: Matched filter for signal in colored noise

3.5   Nuisance Variable

Earlier we saw that the optimum detector in real-valued white Gaussian noise is the matched filter detector. In the derivation however we assumed the noise was real-valued and the optimum time to sample was known. Here we will expand the signal model to contain a complex amplitude signal corrupted with complex Gaussian noise.

$$
\begin{aligned}
x[n] &= v[n] & \text{No Signal Present} \\
x[n] &= \tilde{b}\sqrt{\xi}s[n] + v[n] & \text{Signal Present}
\end{aligned}
\tag{3.22}
$$

In this model $s[n] = 0$ for $n < 0$ and $n \geq M$, $\tilde{b}$ is a complex valued gain, deterministic but unknown. It is assumed $\tilde{b}$, $\mathbf{s}$ and v are independent and $v[n]$ is a zero-mean complex Gaussian random process given by the following pdf

$$
P_V(v) = \frac{1}{(2\pi)^N |\Re_{vv}|} e^{-\frac{1}{2}(\underline{v}-\mu_v)\Re_{vv}^{-1}(\underline{v}-\mu_v)}
\tag{3.23}
$$

If we assume the noise is white complex Gaussian then $|\Re_{vv}| = \sigma_w^2 \mathbf{I}$ and $\mathbf{v} \sim \mathcal{N}(0, \sigma_w^2 \mathbf{I})$. Therefore $\mathbf{x} \sim \mathcal{N}(\tilde{b}\sqrt{\xi}\mathbf{s}, \sigma_w^2 \mathbf{I})$, so the likelihood function is then given by (3.24).

$$
P_X(x|\tilde{b}) = \frac{1}{(2\pi)^N \sigma_w^2 N} e^{-\frac{1}{2\sigma_w^2}(\mathbf{x}-\tilde{b}\sqrt{\xi}\mathbf{s})^H(\mathbf{x}-\tilde{b}\sqrt{\xi}\mathbf{s})}
\tag{3.24}
$$

If we knew $\tilde{b}$ exactly then we would choose the matched filter to be $h_{MF} = \frac{\tilde{b}^*}{\sqrt{\xi}}s^*[-n]$. Since we do not know $\tilde{b}$ we would like to estimate $\tilde{b}$ such that the likelihood function given by (3.24) is maximized. Here, as we did above, it is useful to apply the logarithm operator realizing that maximizing the log-likelihood also maximizes the likelihood function. So we begin by taking the natural log of (3.24).

$$
ln(P_X(x|\tilde{b})) = -ln((2\pi)^N \sigma_w^2 N) - \frac{1}{2\sigma_w^2}(\mathbf{x} - \tilde{b}\sqrt{\xi}\mathbf{s})^H(\mathbf{x} - \tilde{b}\sqrt{\xi}\mathbf{s})
\tag{3.25}
$$

Here we notice that to maximize (3.25) we must minimize the portion of the

function dependant on $\tilde{b}$. Therefore we choose:

$$\hat{\tilde{b}} = \arg\min_{\tilde{b}}(\mathbf{x} - \tilde{b}\sqrt{\xi}\mathbf{s})^H(\mathbf{x} - \tilde{b}\sqrt{\xi}\mathbf{s}) \tag{3.26}$$

Taking the complex gradient with respect to $\tilde{b}^*$ yields (Brandwood, 1983)

$$\nabla_{\tilde{b}^*} = \tilde{b}\xi - \sqrt{\xi}\mathbf{s}^H\mathbf{x} \tag{3.27}$$

finally rearranging and solving for the estimate of $\tilde{b}$

$$\hat{\tilde{b}} = \frac{1}{\sqrt{\xi}}\mathbf{s}^H\mathbf{x} \tag{3.28}$$

Now that we have $\hat{\tilde{b}}$ we can substitute it in for $\tilde{b}$ in our matched filter. The result is (3.29).

$$\hat{\mathbf{h}}_{MF} = \frac{1}{\sqrt{\xi}}\mathbf{s}^H\mathbf{x}\sqrt{\xi}\mathbf{s} = \mathbf{s}^H\mathbf{x}\mathbf{s} \tag{3.29}$$

Applying this estimate of the matched filter gives us a surprisingly simple result. We simply match filter against the transmitted signal and take the magnitude squared of the output. The result is given in (3.30) and depicted in Figure 3-4.

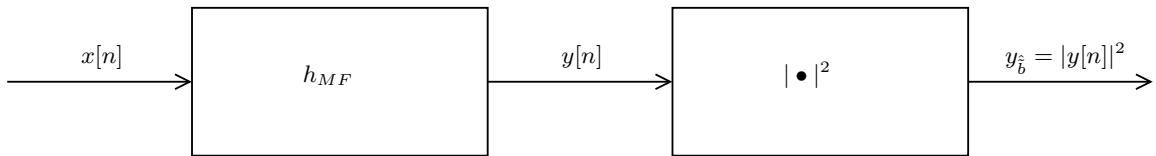$$\text{Filter Output} = \hat{\mathbf{h}}_{MF}^H\mathbf{x} = \|\mathbf{s}^H\mathbf{x}\|^2 \tag{3.30}$$

Figure 3-4: Maximum likelihood filter for unknown $\tilde{b}$

36

3.6 Nuisance Variable Detection Curves

As in the case without nuisance variables we would also like to determine the P_D and P_{FA} so we can generate a ROC. Again we start with the signal description given by (3.22), $\mathbf{v} \sim \mathcal{N}(0, \sigma_w^2 \mathbf{I})$ and $\mathbf{x} \sim \mathcal{N}(\tilde{b}\sqrt{\xi}\mathbf{s}, \sigma_w^2 \mathbf{I})$. We start with the output of the first stage of Figure 3-4 which is given by $\mathbf{y} = \mathbf{s}^H \mathbf{x}$.

$$H_0 : \mathbf{y} = \mathbf{s}^H \mathbf{v}$$
$$H_1 : \mathbf{y} = \mathbf{s}^H(\tilde{b}\sqrt{\xi}\mathbf{s} + \mathbf{v}) \tag{3.31}$$

Since the input to the first stage is a complex Gaussian random variable and the output is simply a sum of complex Gaussian random variables we see that $\mathbf{y}$ is fully described by it's first two moments (Papoulis and Pillai, 2002). Remembering that $\mathbf{s}^H \mathbf{s} = 1$ and taking the expectation of $\mathbf{y}$ and $\mathbf{y}^H \mathbf{y}$ yields the following:

$$H_0 : E[\mathbf{y}] = E[\mathbf{s}^H \mathbf{v}] = 0$$
$$H_1 : E[\mathbf{y}] = E[\tilde{b}\sqrt{\xi}\mathbf{s}^H\mathbf{s}] + E[\mathbf{s}^H\mathbf{v}] = \tilde{b}\sqrt{\xi} \tag{3.32}$$

$$H_0 : var[\mathbf{y}] = N\sigma_v^2$$
$$H_1 : var[\mathbf{y}] = N\sigma_v^2 \tag{3.33}$$

From equations (3.32) and (3.33) above we see that the output of the first stage of the filter is a complex Gaussian random variable with $\mu_y = 0$ for H_0 and $\mu_y = \tilde{b}\sqrt{\xi}$ for H_1. The second stage of the filter takes the magnitude squared of the first stage. Taking the magnitude squared of a complex Gaussian random variable results in a chi-squared (χ_N^2) and non-central chi-squared random variable for H_0 and H_1 respectively. (Papoulis and Pillai, 2002). In each case, the degrees of freedom is equal to 2. The

χ_N^2 density is given by:

$$f_Y(y; k) = \begin{cases} \frac{y^{k/2-1}}{2^{k/2}\Gamma(k/2)} e^{-y/2} & y \geq 0 \\ 0 & \text{otherwise} \end{cases} \tag{3.34}$$

where $\Gamma(\alpha)$ represents the gamma function defined by

$$\Gamma(\alpha) = \int_0^\infty y^{\alpha-1} e^{-y} dy. \tag{3.35}$$

The non-central χ_N^2 density is given by:

$$f_X(x; k, \lambda) = \sum \lim_{i=0}^\infty \frac{e^{-\lambda/2}(\lambda/2)^i}{i!} f_{Y\,k+2i}(x). \tag{3.36}$$

Here, k is the degrees of freedom, λ is the parameter of non-centrality, and the non-central χ_N^2 can be seen as a Poission-weighted mixture of central chi-squared distributions (Papoulis and Pillai, 2002). Using the Neyman-Pearson formulation and varying γ from 0 to ∞ we generate the ROC displayed in Figure 3-5. It is interesting here to compare Figures 3-2 and 3-5. In the case where we knew everything about the signal our probability of detection is higher than the case where we had to estimate $\tilde{b}$. These graphs have been overlaid in Figure 3-6.

3.7   Matched Filter Length

In the previous sections, for convenience, we normalized the signal such that $\mathbf{s}^H\mathbf{s} = 1$ and the transmitted signal was $\sqrt{\xi}\mathbf{s}$ and ξ was the energy in the signal. Here we will alter that definition slightly to look at the effects of the signal transmission length and corresponding matched filter length. For a signal of length N let the total energy in the signal equal ξ where ξ' is the energy in each sample and $\xi = N\xi'$. Substituting
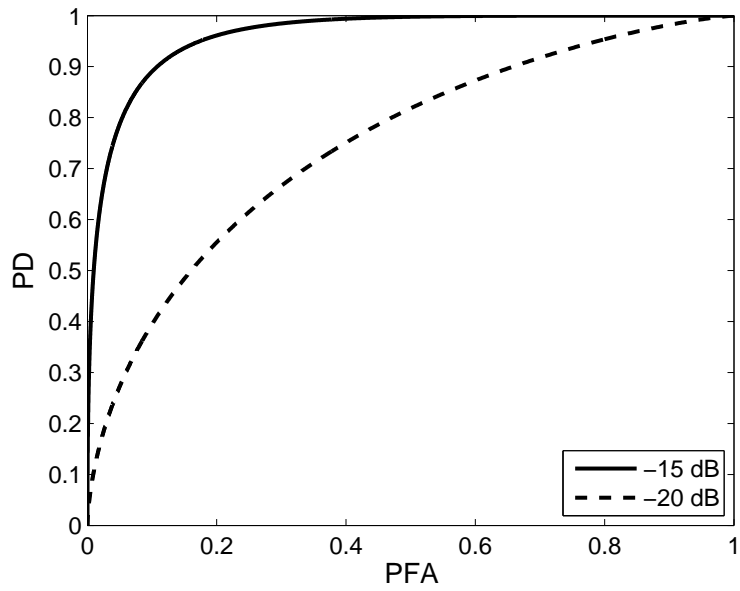
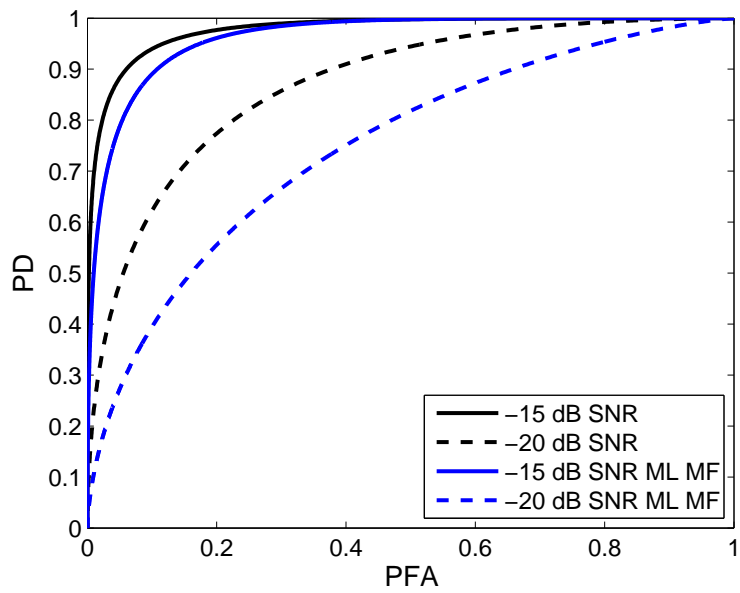Figure 3-5: Maximum Likelihood for matched filter with unknown $\tilde{b}$. MF length N = 127.

Figure 3-6: ROC comparison of clairvoyant MF with MF for unknown $\tilde{b}$

our new value for ξ back into (3.18) we get:

$$H_0 : f_{G|H}(g|H_0) = \mathcal{N}(0, \sigma_w^2)$$
$$H_1 : f_{G|H}(g|H_1) = \mathcal{N}(\sqrt{N\xi'}, \sigma_w^2) \tag{3.37}$$

Here we see that by increasing the matched filter length we can improve our P_D for a given P_{FA} and in an ideal channel that is indeed the case. However that requires that the channel is coherent over the interval corresponding to the length of the matched filter.

3.8   Doubly Spread Channels and the Scattering Function

The ocean channel is bounded by the surface, bottom and other scattering surfaces in between the source and receiver. These multiple reflection surfaces, in addition to refraction due to sound speed variability, create a multipath environment in which the transmitted signal is received in multiple time delays. These channels are referred to as *delay spread* channels (Van Trees, 2001). Motion in the source, receiver, or any of the scattering surfaces can cause a signal transmitted at a single frequency to be received at multiple frequencies. These channels are referred to as *Doppler spread* channels (Van Trees, 2001). Channels that are spread in both Doppler and delay are called *doubly spread* channels (Van Trees, 2001).

The channel scattering function physically represents the power spectrum of the reflection process (Van Trees, 2001). As a power spectrum, it is real and non-negative. It is characterized by the statistics of the reflection process. In the absence of knowing the channel scattering statistics, an estimate of the scattering function for the channel can be created by thinking of the channel as a tapped delay line, with complex scattering weights. The output of a linear filter that is matched to the signal is a faithful representation of the channel, when the added noise is white (Turin, 1960). Therefore

filtering the received signal with a bank of Doppler shifted matched filters will result in an estimate of the scattering function for each delay and Doppler frequency. An example scattering function estimate is shown in Figure 3-7.
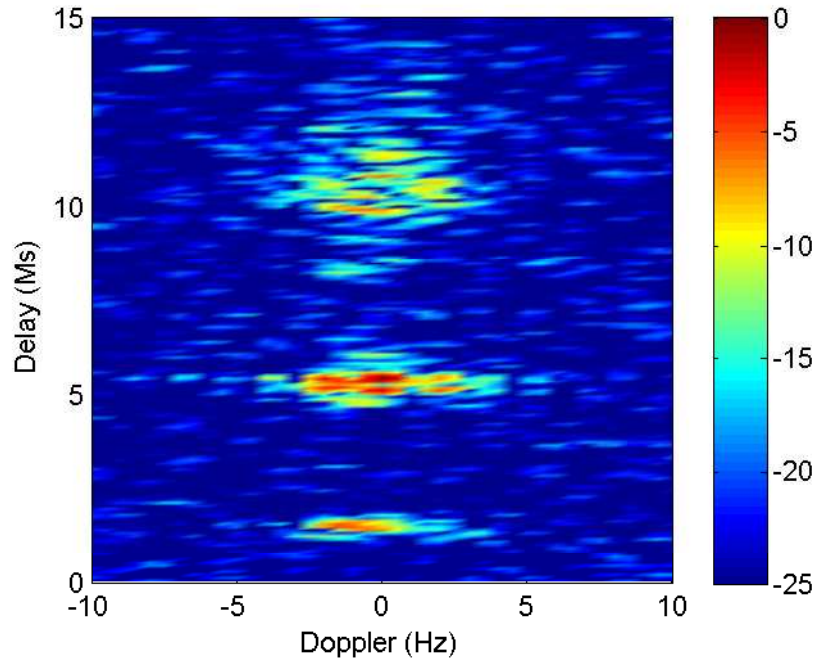

Figure 3-7: A shallow water channel scattering function from KAM11 experiment, JD182 0203Z. The depth of water was approximately 100 m over a source to receiver range of 7 km. Environmental conditions include low to moderate winds with some swell and choppy waves.

3.9   Ambiguity Function

The development of the matched filter to this point has relied on two subtle assumptions: known (or very small) signal delay and zero Doppler shift. Since we derived in Section 3.2 that the output of the optimum linear filter was maximized when the filter is matched to the signal, any discrepancy in signal delay or Doppler shift will reduce the output of the MF. It is important to look at these two effects when designing signals. The standard method for evaluating these effects is through the *ambiguity function*.

The Doppler effect can be introduced by a moving source, receiver or both. Ad-

ditionally, a change in path length in the channel due to its time variability can also cause a Doppler shift. For a simple example, in the case of a stationary source and moving detector, the change in frequency due to Doppler shift is given by:

$$f_{\mathrm{d}} = -f_0\left(\frac{v}{c}\right). \tag{3.38}$$

Here, f_0 is the carrier frequency, c is the speed of sound in water and v is the velocity of the detector. To match the filter to the Doppler shifted signal, the linear filter must be Doppler shifted by the same amount. The MF for the received signal is now given by:

$$h_{\mathrm{MF}} = s^*[-n]e^{(j2\pi\frac{f_{\mathrm{d}}}{f_s}n)}. \tag{3.39}$$

Let $\hat{f}_{\mathrm{d}}$ be the estimate of the Doppler shift and $\Delta f = f_{\mathrm{d}} - \hat{f}_{\mathrm{d}}$ be the difference between the true Doppler shift and the estimate. Let n_0 be the time delay from source to receiver (in samples), then the output for the signal portion of the MF given by Figure 3-4 is

$$y[n] = \xi\|\tilde{b}\|^2 \quad \|\sum_{k=0}^{N-1} s^*[-k]s[n - n_0 - k]e^{(j2\pi\frac{\Delta f}{f_s}k)}\|^2 \tag{3.40}$$

or in the continuous time equivalent, where τ_0 is the time delay:

$$y(t) = \xi\|\tilde{b}\|^2 \quad \|\int s^*(-\tau)s(t - \tau_0 - \tau)e^{(j2\pi\Delta f\tau)}d\tau\|^2. \tag{3.41}$$

Neglecting the scaling factor and letting $\Delta\tau = t - \tau_0$, (3.41) can be written as a function of $\Delta\tau$ and Δf.

$$\Theta(\Delta\tau, \Delta f) = \|\int s^*(\tau + \frac{\Delta\tau}{2})s(\tau - \frac{\Delta\tau}{2})e^{(j2\pi\Delta f\tau)}d\tau\|^2 \tag{3.42}$$

(3.42) is called the ambiguity function. It is the squared magnitude of the time-frequency auto-correlation function. The ambiguity function is a measure of the degree of similarity between a complex envelope and a replica of it that is shifted in

42

time and frequency (Van Trees, 2001).

3.9.1 The Square Pulse

Before looking at the properties of the ambiguity function it is useful to look at several examples. To start we will look at the simplest example, the square pulse. Two illustrative examples are the cases for zero Doppler error and zero delay error. In the case with zero Doppler error, (3.42) reduces to the squared magnitude of the time auto-correlation function. For a simple square pulse, the time auto correlation function is a triangle, and its square is the warped triangle shown in Figure 3-8. In the case for zero delay, (3.42) reduces to the magnitude squared Fourier transform of the squared magnitude of the signal. These two cases and the full ambiguity function are shown below in Figure 3-8.

3.9.2 Linear Frequency Modulated Chirp

The linear frequency modulated (LFM) chirp is a wave form that has been modulated in frequency. If we start with the square pulse s(t) given in the previous section, then the chirped pulse is given by (3.43).

$$s_{\text{LFM}}(t) = s(t)e^{j2\pi\mu t^2/2} \tag{3.43}$$

Since we are frequency modulating the square pulse, which has real-valued complex envelope, the phase of the chirped square pulse is just $2\pi\mu t^2/2$. Taking the derivative yields the instantaneous frequency of $2\pi\mu t$. It is a linear function in time, hence the name *linear* frequency modulated.

The parameter μ controls the rate at which the frequency of the chirp increases as the slope of the linear instantaneous frequency function. For a given pulse length, increasing μ will increase the bandwidth of the chirped signal. As the bandwidth of the signal increases, the accuracy with witch the signal delay can be estimated improves (Van Trees, 2001). The bandwidth is approximately the product of μ and the pulse duration. The LFM chirp, for a bandwidth of 1200 Hz and 127 ms pulse

(a) $\Delta f = 0$

(b) $\Delta \tau = 0$
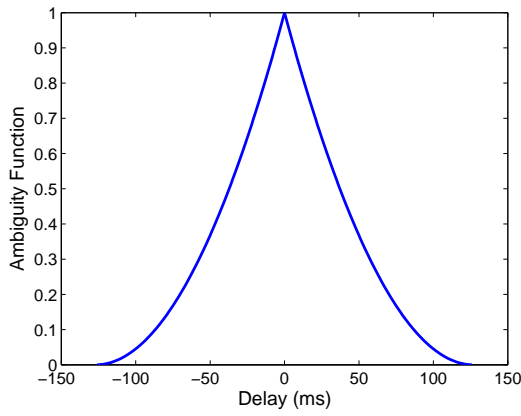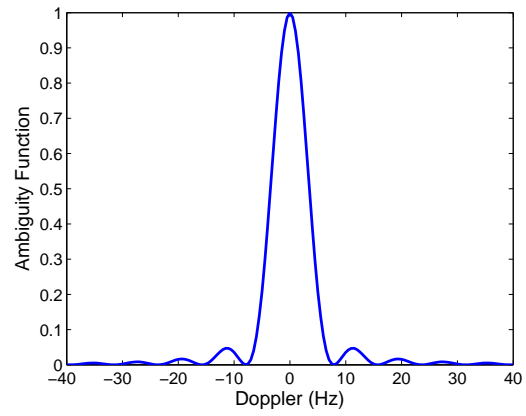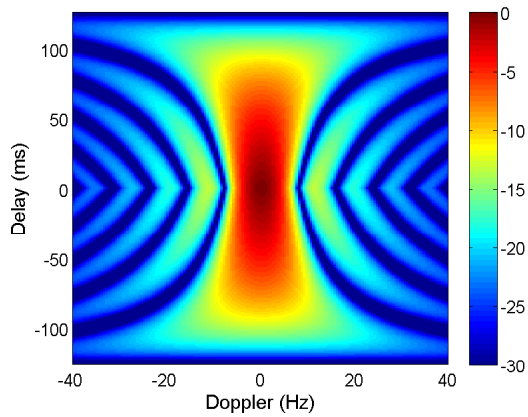
(c) Ambiguity Function

(d) Complex Envelope

Figure 3-8: Ambiguity function for a 127 ms square pulse. Figure (a) is a vertical slice of the ambiguity function for zero Doppler error. Figure (b) is a horizontal slice of the ambiguity function for zero delay error. Figure (c) is the full ambiguity function for a range of delay and Doppler errors.
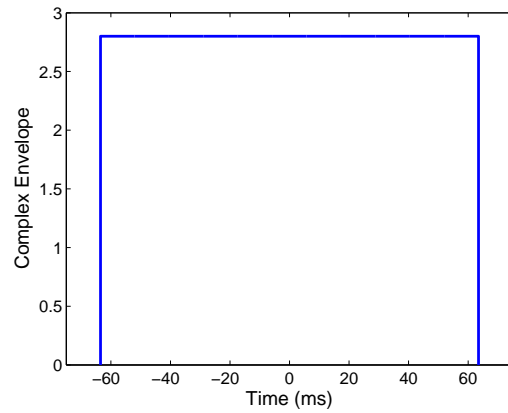
(a) $\Delta f = 0$

(b) $\Delta \tau = 0$

(c) Ambiguity Function

(d) Complex Phase
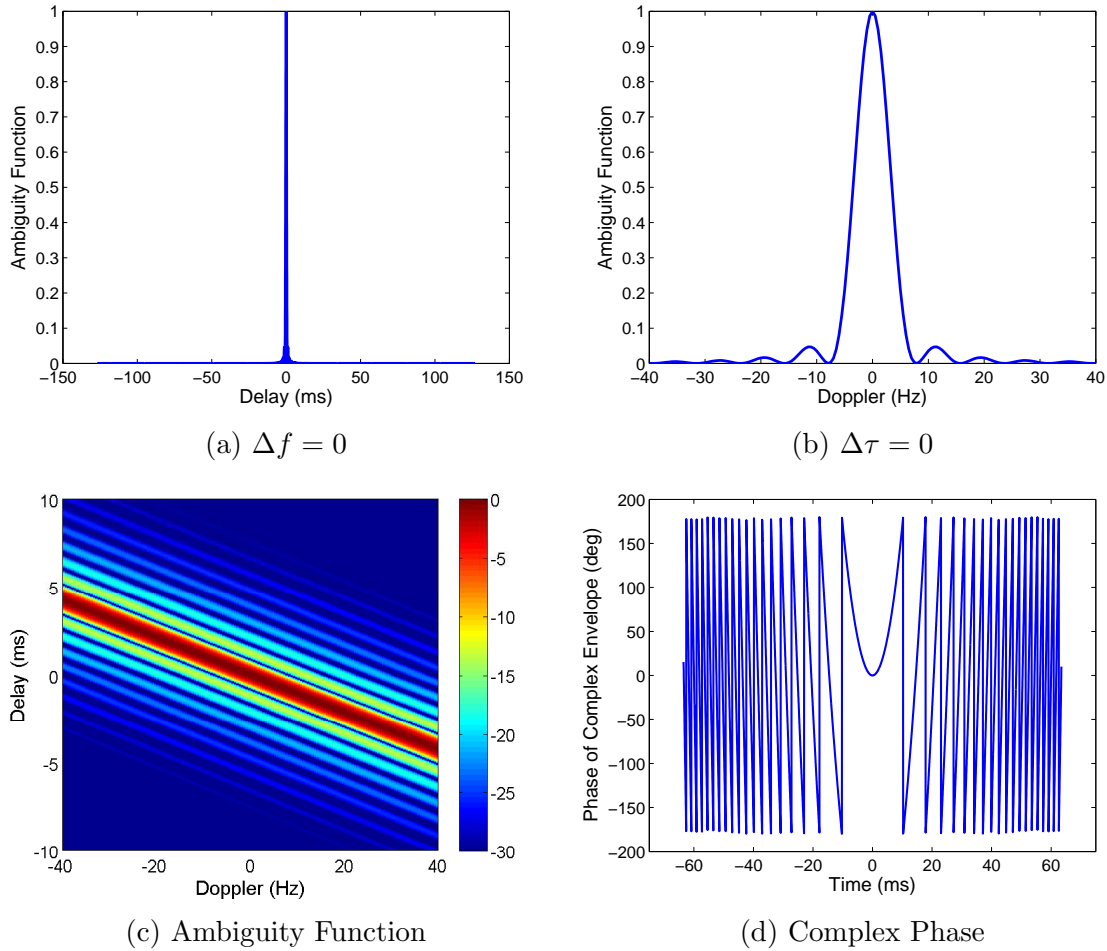
Figure 3-9: Ambiguity function for a 127 ms LFM chirped square pulse. Figure (a) is a vertical slice of the ambiguity function for zero Doppler error. Figure (b) is a horizontal slice of the ambiguity function for zero delay error. Figure (c) is the full ambiguity function for a range of delay and Doppler errors.

duration, are shown in Figure 3-9. Notice in the two dimensional ambiguity function the LFM pulse has been sheared in frequency when compared to the square pulse. For a given Doppler frequency, the cross correlation of the chirp has a much narrower mainlobe, but for a given delay, the mainlobe of the ambiguity function is as broad in Doppler as the square pulse. This effect is clearly visible when comparing Figures 3-9 and 3-8. This property of the LFM chirp allows it to be tolerant to a Doppler shifted signal while still producing sharp detection peaks.

3.9.3 The Maximum Length Sequence

The Maximum Length Sequence (MLS), or m-sequence are often called pseudo-random sequences. The random comes from the fact that they have many properties of a Bernoulli sequence, most importantly of which is the similarity in their auto-correlation functions (Van Trees, 2001). They are *pseudo* because the sequences are not random at all, but completely deterministic. The term *maximum length* derives from the fact that for all integer values N there exists a sequence that has a period of $L = 2^N - 1$. Additionally, these sequences are often called maximum length *shift register* sequences for how they are generated. A L length MLS can be generated by a series of N shift registers with specific feedback connections, see Proakis chapter 8 for a table of stage connections.

The desirable property of m-sequences, for signal detection, is their auto-correlation. To get maximal benefit of this auto-correlation, a m-sequence should be cross-correlated with a repeated version of itself, or circularly auto-correlated. The circular correlation is required for maximal sidelobe suppression. For a normalized MLS sequence with length L, in the circular auto-correlation, the mainlobe peak will attain unity while the side lobes will approach $1/L$. Figure 3-10 contains the zero Doppler slice, zero delay slice, and the full ambiguity function.

3.9.4 Ambiguity Function Properties

The ambiguity function contains many properties, only a short subset will be discussed here. For a complete discussion see (Van Trees, 2001) chapter 10.

Property 1 (Shear): If:

$$s_1(t) \implies \Theta(\Delta\tau, \Delta f) \tag{3.44}$$

then:

$$s_2(t) \equiv s_1(t)e^{j2\pi\mu\frac{t^2}{2}} \implies \Theta(\Delta\tau, \Delta f - \mu\Delta\tau) \tag{3.45}$$

This property can be derived by substituting $s_2(t)$ in for $s(t)$ in (3.42). The end result is that, modulation of a signal by a linear sweep in frequency produces an ambiguity

(a) $\Delta f = 0$

(b) $\Delta \tau = 0$
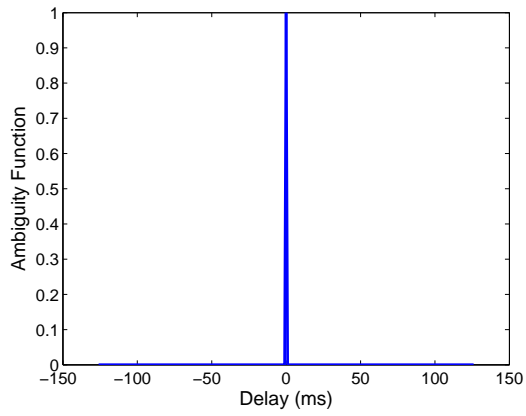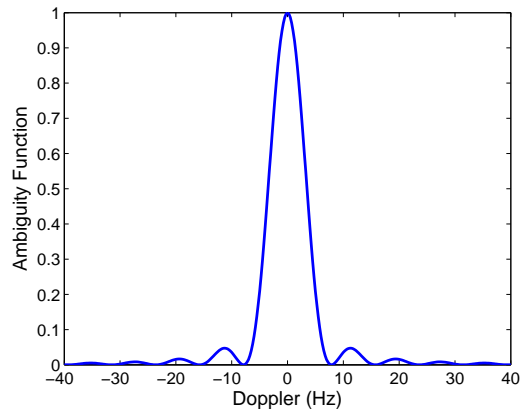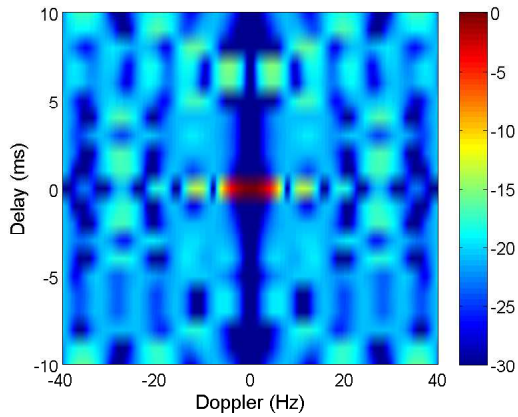
(c) Ambiguity Function
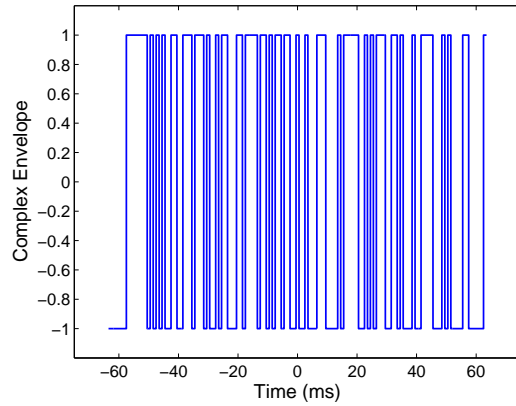
(d) Complex Envelope

Figure 3-10: Ambiguity function for a 127 ms MLS with $N = 7$ and $L = 127$. Figure (a) is a vertical slice of the ambiguity function for zero Doppler error. Figure (b) is a horizontal slice of the ambiguity function for zero delay error. Figure (c) is the full ambiguity function for a range of delay and Doppler errors.

function that is sheared in the frequency axis (Van Trees, 2001). This is apparent when comparing Figures 3-9 and 3-8.

Property 2 (Peak Value):

$$\Theta(0,0) = 1 = \text{Max Value} \tag{3.46}$$

Again, using (3.42) and substituting in for zero delay and Doppler shift, we see that the ambiguity function reduces to the inner product of the signal. Noting that the complex envelopes have been normalized and utilizing the Cauchy-Schwartz inequality we see that property 2 must hold.

Property 3 (Volume Invariance):

$$\int_{-\infty}^{\infty} \int_{-\infty}^{\infty} \Theta(\Delta\tau, \Delta f) d\tau df = 1 \tag{3.47}$$

This is perhaps one of the more important properties of the ambiguity function. It states that the volume under the ambiguity function is independent of the signal choice. Therefore if a signal is chosen to reduce the mainlobe width, that volume will be shifted to the sidelobes. For this reason, the property is also often referred to as the *uncertainty principle* (Van Trees, 2001). This shift in volume is evident when comparing Figures 3-8, 3-9 and 3-10.

3.9.5   Signal Design

From the derivation of the matched filter is was determined that the probability of detection was only a function of the SNR and not the shape of the signal. However, that assumption assumed a perfectly Doppler matched (or zero Doppler shifted channel) matched filter that sampled with zero delay error. The ambiguity function discussion illuminates how a signal is effected for Doppler estimate error or delay error.

The MLS sequence most closely represented the ideal ambiguity function of an impulse at the origin, however it is not very Doppler tolerant. This intolerance though

makes it a good candidate for estimating Doppler via a bank of Doppler shifted matched filters. The LMF chirped pulse on the other hand is more Doppler tolerant, but introduces a delay Doppler uncertainty, i.e. it is unable to jointly estimate Doppler and delay. These trade-offs must be considered when choosing an appropriate signal.

3.10 Coherence Length

In Section 3.7 it was shown that the gain of the MF was dependent of the signal length. However, that required that the MF be coherent at all lengths. The channel depicted in Figure 3-7 exhibits approximately 8 Hz of Doppler spread. A simple model that illustrates how this spread may effect the matched filter performance is the Doppler shifted signal. The received signal is now given by:

$$x[n] = e^{j\theta n}s[n] + v[n] \tag{3.48}$$

where θ is the Doppler frequency divided by the sampling rate. Each sample is multiplied by unit magnitude vector with increasing phase. As the length of the matched filter grows, larger phase shifts are averaged in, and eventually as the phase shift passes π where continued averaging will reduce the gain of the matched filter. This can be seen pictorially in Figure 3-11. For this thesis we will consider the peak of the first lobe is the coherence length of the channel. This is the point for which choosing a filter length longer than this will result in a reduced output of the MF. The model displayed here does not fully capture the effect of Doppler on a signal or represent all channel coherence issues but merely illuminates how channel coherence issues can reduce the gain of the matched filter.
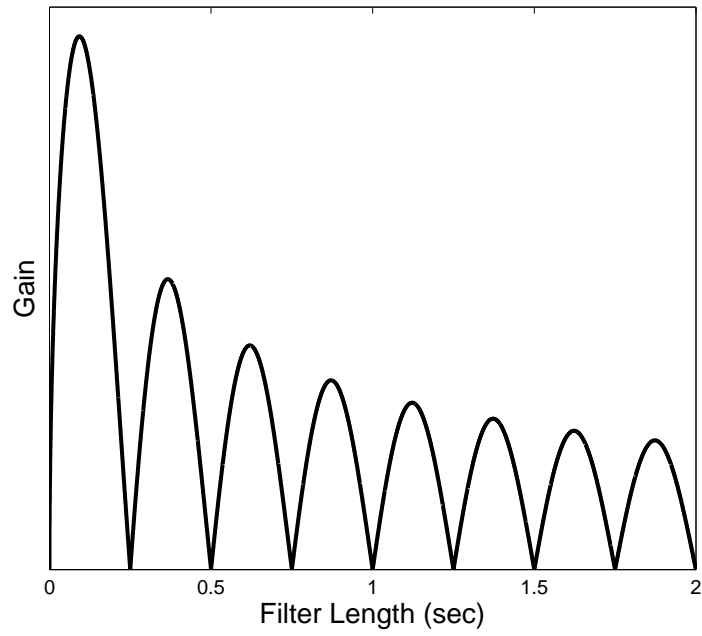
Figure 3-11: MF gain versus filter length for a 4 Hz Doppler shifted channel.

Chapter 4

Adaptive Detection

4.1 Introduction

This chapter will describe the proposed adaptive detector. However, it is first useful to look at the construction of a linear adaptive equalizer and its common uses. In a general communications scheme we would like to take our desired message, transmit it to our receiver and have that receiver be able to recreate the original desired message.

The distortion or change in the signal from transmitter to receiver is caused by the channel. In the absence of noise, and with perfect knowledge of the channel, we would simply invert the channel effect and be left with our original transmitted signal. In real world scenarios however, noise is present and attempting to invert the channel is not a good solution because the inverse filter accentuates exactly the frequencies where the signal power is small relative to that of the noise (Oppenheim and Verhese, 2010).

This chapter is laid out two major areas. Sections 4.2, 4.3, 4.4, 4.5 and 4.6 develop the basic feedforward linear adaptive equalizer based on a recursive least squares algorithm. The second half of the chapter is concerned with the adaptive detector. Section 4.7 develops the ALED. Section 4.8 expands the ALED to handle multiple element arrays. Finally, Section 4.9 suggests a logical argument for why the ALED is able to achieve good results.

4.2   Linear Equalizer

In a linear equalizer we attempt to remove the channel effects with the use of a linear filter. The goal is to achieve the ideal transmission medium when cascading the effects of the channel with the linear filter (Haykin, 2002). If the channel is fixed in time, the weights of the linear filter are also fixed, if the channel is time varying, the channel weights need to adapt to the changing channel. The output of the linear filter or linear adaptive filter is an estimate of the transmitted data. Since the output is only an estimate, the difference in the output and the channel input is the error. The equalizer attempts to minimize this error in some sense. Figure 4-1 shows the block diagram of an adaptive equalizer.

There are several criteria we could use to minimize the error. One desirable method minimizes the sum of the squared error over the interval of interest. This method is known as the *method of least squares.* It is desirable because it leads to a computationally efficient recursive algorithm that is useful in time-varying channels.
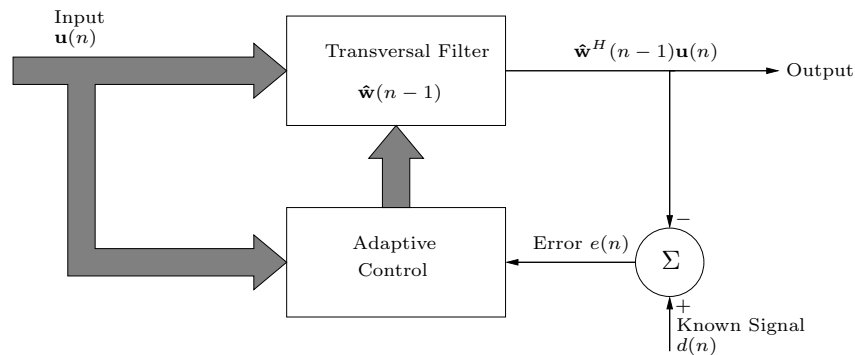

Figure 4-1: Linear Adaptive Equalizer

4.3   Method of Least Squares

In the method of least squares we wish to minimize the squared difference between our desired signal $d(n)$ and our signal estimate $\hat{d}(n)$. If the input to the transversal filter is $u(n)$ (see Figure 4-2) and the tap weights are given by w_i^* for $i = 0, 1, \ldots, M - 1$,

then the output of the filter is given by

$$y(n) = \sum_{l=0}^{M-1} w_l^* u(n-l). \tag{4.1}$$

Specifying the error $e(n)$ to be the difference between $d(n)$ and the filter output yields

$$e(n) = d(n) - \sum_{l=0}^{M-1} w_l^* u(n-l). \tag{4.2}$$

Finally, as stated above, we wish to estimate the tap weights that will minimize the squared error.

$$(\hat{w}_0, \hat{w}_1, \hat{w}_2, \ldots, \hat{w}_{M-1}) = \arg\min_{\tilde{b}} \sum_{j=j_1}^{j_2} |e(j)|^2 \tag{4.3}$$

Here, j is range of time values over which we wish to minimize the error. Moving into vector form, let

$$\hat{\mathbf{w}} = (\hat{w}_0, \hat{w}_1, \hat{w}_2, \ldots, \hat{w}_{M-1})^T \tag{4.4}$$

$$\mathbf{u_j} = (u(j), u(j-1), u(j-2), \ldots, u(j-M+1))^T, \tag{4.5}$$

and substituting back in to (4.3) yields:

$$\hat{\mathbf{w}} = \arg\min_{\mathbf{w}} \sum_j (d(j) - \mathbf{w}^H \mathbf{u_j})(d(j) - \mathbf{w}^H \mathbf{u_j})^*. \tag{4.6}$$

Taking the complex gradient (Brandwood, 1983) with respect to $\mathbf{w}^H$ and setting equal to zero simplifies to:

$$\left(\sum_j \mathbf{u_j} \mathbf{u_j}^H \right) \mathbf{w} - \sum_j \mathbf{u_j} d^*(j) = 0 \tag{4.7}$$

letting

$$\mathbf{\Phi} = \sum_j \mathbf{u_j u_j}^H \tag{4.8}$$

where $\mathbf{\Phi}$ is the M by M the sample correlation matrix and

$$\mathbf{z} = \sum_j \mathbf{u_j} d^*(j) \tag{4.9}$$

where $\mathbf{z}$ is the sample cross correlation vector between the desired response $d(j)$ and $\mathbf{u_j}$. Substituting (4.8) and (4.9) into (4.7) yields the familiar least squares estimate for $\mathbf{w}$:

$$\hat{\mathbf{w}} = \mathbf{\Phi}^{-1}\mathbf{z} \tag{4.10}$$

(4.10) assumes the existence of $\mathbf{\Phi}^{-1}$ i.e. $\mathbf{\Phi}$ is not singular.
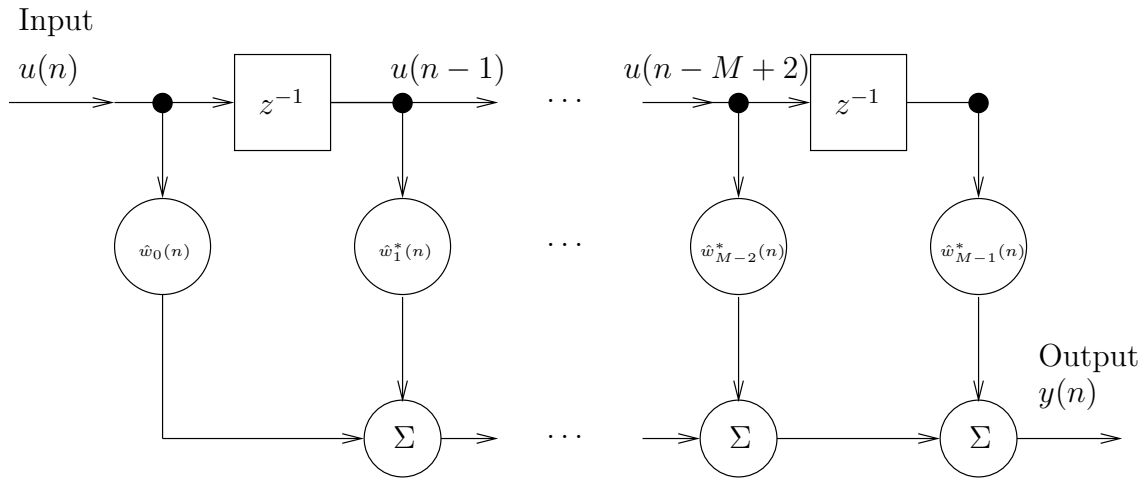

Figure 4-2: Linear Transversal Filter

4.4 Recursive Least Squares

In the previous section, (4.10) was the solution for the linear transversal filter tap weights where the channel was constant over an interval of time j. In ocean acoustics however, the channel is time varying, so the desire is that the tap weights will adapt

to the changing channel. Therefore we wish to update our estimate of the filter tap weights given our estimate of the filter tap weights, $\hat{\mathbf{w}}$, at time $n-1$ and the updated data at time n. Furthermore it is obvious that it is desirable to weight the more recent information more heavily. Implementing these two objectives gives the following replacements for (4.8) and (4.9), the sample correlation matrix and the sample cross correlation vector respectively (see (Haykin, 2002) chapter 9 for full derivation).

$$\mathbf{\Phi}(n) = \sum_{j=1}^{n} \lambda^{n-j} \mathbf{u}(j) \mathbf{u}^H(j) + \delta \lambda^n \mathbf{I} \qquad (4.11)$$

$$\mathbf{z}(n) = \sum_{j=1}^{n} \lambda^{n-j} \mathbf{u}(j) d^*(j) \qquad (4.12)$$

where λ, such that $0 < \lambda < 1$, provides an exponentially decaying weight on previous data. The second term in (4.11) diagonally loads the correlation matrix ensuring $\mathbf{\Phi}(n)$ is nonsingular at all stages of the computation (Haykin, 2002). In matrix notation these equations simplify to: (Haykin, 2002)

$$\mathbf{\Phi}(n) = \lambda \mathbf{\Phi}(n-1) + \mathbf{u}(n) \mathbf{u}^H(n), \qquad (4.13)$$

$$\mathbf{z}(n) = \lambda \mathbf{z}(n-1) + \mathbf{u}(n) d^*(n). \qquad (4.14)$$

From (4.13) and (4.14), the current sample correlation matrix and sample cross correlation vector, it is easy to see the recursive update. However, due to the recursive nature, the update equations must be initialized. The sample correlation matrix is diagonally loaded with a small value δ, see Haykin Chapter 9 (Haykin, 2002) for more information on choosing this value. The sample cross correlation vector is initialized by setting $\mathbf{w}(0)$ to zero, which is the product of $\mathbf{\Phi}^{-1}(0)$ and $\mathbf{z}(0)$.

4.5 RLS Algorithm

Direct implementation of (4.10) is computationally expensive. If $\mathbf{\Phi}$ is an N by N matrix, inverting $\mathbf{\Phi}$ is an order N^3 operation, $O(N^3)$. To reduce to computational complexity to $O(N^2)$ we apply the matrix inversion lemma, also know as Woodbury's Identity, given by the following relation (Haykin, 2002):

if

$$\mathbf{A} = \mathbf{B}^{-1} + \mathbf{C}\mathbf{D}^{-1}\mathbf{C}^H \tag{4.15}$$

then

$$\mathbf{A}^{-1} = \mathbf{B} - \mathbf{B}\mathbf{C}(\mathbf{D} + \mathbf{C}^H\mathbf{B}\mathbf{C})^{-1}\mathbf{C}^H\mathbf{B}. \tag{4.16}$$

Letting:

$$\mathbf{A} = \mathbf{\Phi}(n),$$
$$\mathbf{B}^{-1} = \lambda\mathbf{\Phi}(n-1),$$
$$\mathbf{C} = \mathbf{u}(n),$$
$$\mathbf{D} = 1 \tag{4.17}$$

and using (4.15), (4.16), (4.14) and (4.13) we can expand (4.10) into a computationally efficient recursive least squares (RLS) algorithm. For a full derivation of the algorithm see chapter 9 of Haykin's *Adaptive Filter Theory*.

The RLS algorithm forms the heart of the adaptive detector proposed by this thesis. Haykin's algorithm has been reproduced for convenience in Table 4.1 and is demonstrated pictorially in Figure 4-1. In the algorithm, for simplicity of notation, $\mathbf{P}(n)$ has been substituted for $\mathbf{\Phi}(n)^{-1}$ and $\mathbf{k}(n)$ is called the gain vector because weights the updates to $\hat{\mathbf{w}}$ and $\mathbf{P}$. The adjustable parameters of the algorithm are δ, N and λ.

RLS Algorithm

Initialize:
$$\hat{\mathbf{w}}(0) = \mathbf{0}$$
$$\mathbf{P}(0) = \delta^{-1}\mathbf{I}$$

For each iteration, $n = 1, 2, \ldots$ compute:
$$\boldsymbol{\pi}(n) = \mathbf{P}(n-1)\mathbf{u}(n),$$
$$\mathbf{k}(n) = \frac{\pi}{\lambda + \mathbf{u}^H(n)\boldsymbol{\pi}(n)},$$
$$e(n) = d(n) - \hat{\mathbf{w}}^H(n-1)\mathbf{u}(n),$$
$$\hat{\mathbf{w}} = \hat{\mathbf{w}}(n-1) + \mathbf{k}(n)e^*(n),$$
and
$$\mathbf{P}(n) = \lambda^{-1}\mathbf{P}(n-1) - \lambda^{-1}\mathbf{k}(n)\mathbf{u}^H(n)\mathbf{P}(n-1).$$

Table 4.1: Haykin's RLS Algorithm

The forgetting factor λ exponentially weights the previous data and the inverse of $1 - \lambda$ is approximately a measure of the *memory* of the algorithm (Haykin, 2002). The regularization parameter δ is used to initialize the inverse correlation matrix. Finally, N is the number of taps in the transversal filter. Its length is set to capture the important time dispersed arrivals of the signal, but limited in length to minimize the noise in the inverse correlation matrix.

4.6   RLS Equalizer

In the communications scheme detailed above the RLS algorithm is used to adapt the equalizer filter coefficients to undo the effects of a time varying channel. Given the received signal containing the channel corrupted data and the desired data signal it can estimate the linear transversal tap weights that will give the least squares estimate to the transmitted data. However for this to work it requires knowledge of where in the received signal the data exists and a copy of the transmitted data.

The copy of the transmitted data is often called *training data* since it is used to train the equalizer in training mode. The equalizer will use this data to get an estimate of the transversal filter weights. The equalizer is then shifted to decision

directed mode where it will now use its estimate of the data as the known data (Haykin, 2002). This shift in modes is what allows it to receive new messages.

The second piece of information the equalizer needs is the location of the data. Locating this piece of data is called frame synchronization or just synchronization. The most common method of synchronization is done by transmitting a probe usually an LFM chirp or MLS, and then using a MF to locate the start of the probe, as is done in (Stojanovic et al., 1994).

Other variants on the RLS equalizer exist (Decision Feedback Equalizers, Turbo Decoders, etc...) but are not pertinent to this thesis and will not be discussed further.

4.7 Adaptive Linear Equalizer Detector

4.7.1 Decision Device

In a MF detector, as discussed in Chapter 3 of this thesis, the detector processes the received signal with a linear filter that is matched to the signal, the resultant output is maximal when the signal is present. This magnitude, or squared magnitude, of the output is compared to a threshold γ, and a decision is made on whether or not the transmitted data is contained in the received signal. In the adaptive linear equalizer detector (ALED), the proposed threshold comparison is not done with the value of the output, but with the BER.

The ALED at its core is a linear equalizer in training mode. The equalizer, as described above, given the input vector and training data, estimates the filter weights that minimize the squared error, where the error is given by:

$$e(n) = d(n) - \hat{\mathbf{w}}^H(n-1)\mathbf{u}(n). \tag{4.18}$$

The initial decision estimate of the data, $\hat{\mathbf{w}}^H(n-1)\mathbf{u}(n)$, is called the *soft* decision or $\hat{d}_{soft}(n)$. The soft decision is complex in value where the training data (in an assumed binary scheme) only contains values of 1 or −1. The soft decision is then passed into a *decision device* or threshold device that determines if $\hat{d}_{soft}(n)$ more

likely represents a 1 or -1. In the case where *a priori* probabilities of the two values are equal, the decision device simply assigns values of 1 or -1 if the real part of $\hat{d}_{soft}(n)$ is greater than or less than zero respectively.
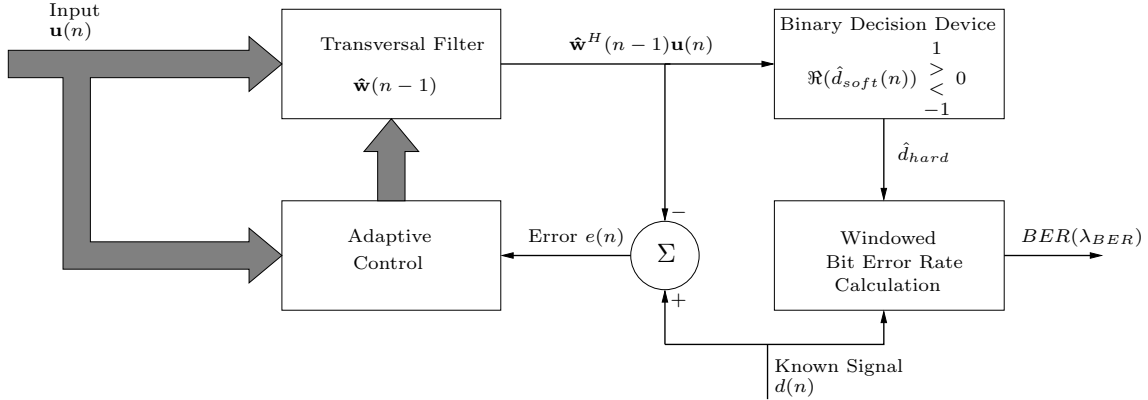

Figure 4-3: Linear adaptive equalizer with windowed BER calculation

Once the hard decision has been determined a bit error rate (BER) calculation can be completed. A batch BER calculation can be made by dividing the total number of symbol errors by the total number of transmitted symbols. The BER is a measure of the equalizers performance, its ability to undo the effects of the channel and recover the transmitted data. If an equalizer is given a pure noise signal at its input, then its BER should average out over time to approximately 50 percent. If the signal is present in the noise, the average BER should be something less than 50 percent. The threshold γ can be set to a level below 50 percent, determined by an acceptable P_{FA}. As the BER drops below the specified threshold, a detection is flagged.

Now in general, BERs are calculated in batch form after all processing is completed. Since the goal is to detect the incoming signal in real time, a windowed BER calculation is desired. The ALED in this thesis uses an exponentially weighted window with $0 < \lambda_{BER} < 1$ and the BER given by the following equation:

$$BER(n) = \lambda_{BER}BER(n-1) + (1 - \lambda_{BER})\epsilon_{symbol} \tag{4.19}$$

and ϵ_{symbol} is given by:

$$\epsilon_{symbol} = \begin{cases} 0 & \text{current symbol correct} \\ 1 & \text{current symbol incorrect} \end{cases} \tag{4.20}$$

Figure 4-3 demonstrates a block diagram implementation of the real time BER calculation.

4.7.2 Hard Decision Improvement

In the previous section each hard decision was made based on one soft decision. This method will allow for minimum time lag between signal reception and data detection. If it is acceptable to introduce a small time lag into the detection, it is beneficial to evaluate multiple soft decisions prior to making the hard decision.

Each soft decision can be thought of as a sample of of a random process with some mean μ and variance σ^2, each independent and identically distributed. The mean in this case should be one of two possible values 1 or -1. The sample mean is given by (4.21).

$$M_N = \frac{\hat{d}_{soft1} + \hat{d}_{soft2} + \ldots + \hat{d}_{softN}}{N} \tag{4.21}$$

Here, M_N is itself a random variable with:

$$E[M_N] = \mu \tag{4.22}$$

and

$$var(M_N) = \frac{\sigma^2}{N} \tag{4.23}$$

By the weak law of large numbers, the sample mean will converge to the true mean as N increases to ∞ (Papoulis and Pillai, 2002). This is apparent from (4.23) where we see the variance of the estimate is reduced as N increases. Therefore if we average enough soft decisions the hard decision will converge to the true signal value.

4.7.3 Parallel Processing

As mentioned in Section 4.6 an equalizer requires frame synchronization or knowledge of where the signal starts. An alternative method is a brute force parallel processing attack on the data. This requires that a receiver assumes each point in time is the data start point, and then assigns an equalizer to process that received signal. The equalizer that is correctly aligned with the data will begin to converge to useful tap weight estimates and the BER of its output will drop below 0.5. It is this last thought that leads to the design of the ALED.

An alternative brute force approach, rather than starting an equalizer at each point in time, is to start all equalizers at the same point in time with different assumed points in the known signal. In this subtle change it is now easy to see that the number of required parallel equalizers is reduced to L, where L is the length of the data sequence. If the ALED is to be used as a front end detector (its rightful place in the communication scheme), L will be the length of the detection sequence. The number of parallel equalizers can be further reduced by using a detection sequence that contains repetitive signals. For a detection sequence of length L containing R signal repetitions the number of required parallel equalizers is now L/R.

As discussed in Section 4.5 the RLS algorithm is computationally $O(N^2)$. This computational expense arises from inverting the sample correlation matrix. The key fact the ALED is capitalizing on is that each of the parallel equalizers can utilize the same inverse sample correlation matrix and gain vector. Therefore each equalizer is only responsible for updating the tap weight vectors based on its own error. This is only $O(N)$. Figure 4-4 is a block diagram representation of the ALED.

4.8 Multiple Channels

To this point, all derivations has assumed a single input channel. However, no generality has been lost with this assumption. In the case with multiple channels, the received vectors are simply stacked into the input vector $\mathbf{u}$. For example, in the case of L channels each with M taps, the input vector becomes:
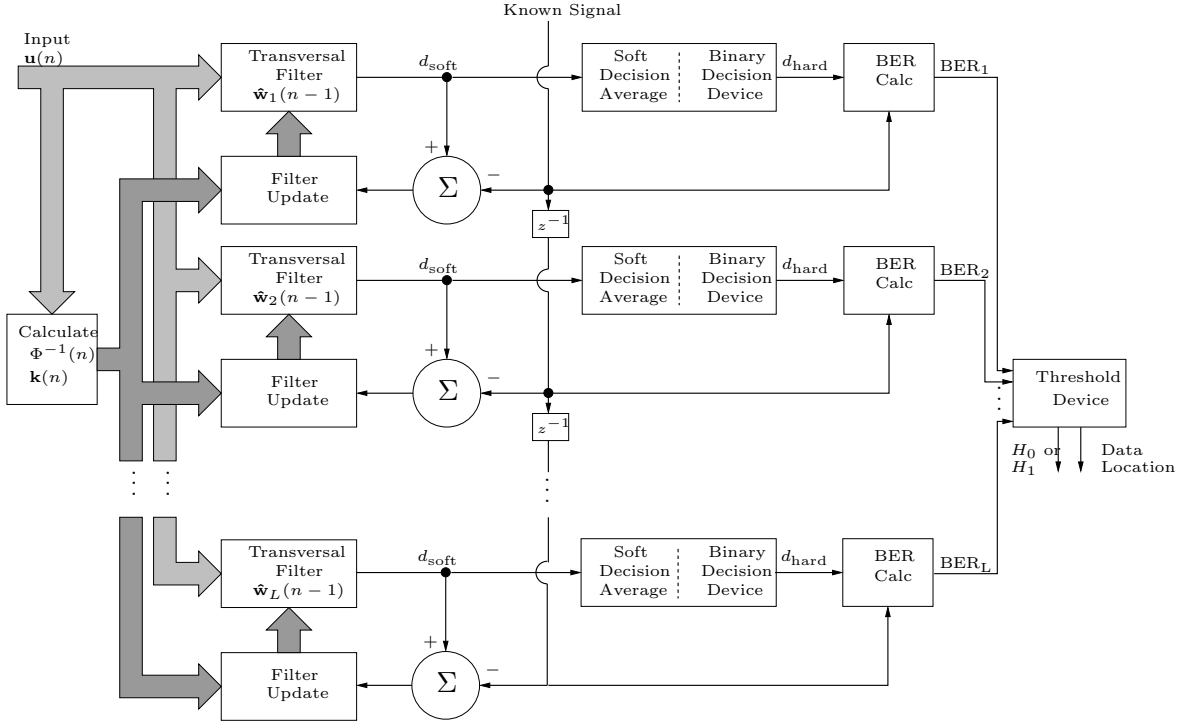
Figure 4-4: Adaptive Linear Equalizer Detector (ALED)

$$\mathbf{u} = [\mathbf{u}_{\text{CHAN1}}, \mathbf{u}_{\text{CHAN2}}, \ldots, \mathbf{u}_{\text{CHANL}}]^T \qquad (4.24)$$

In the case of an acoustic array, where each hydrophone represents a channel, the matrix $\mathbf{\Phi}$ now represents a space-time sample correlation matrix instead of merely a temporal sample correlation matrix. Again solving the least squares (4.10), we arrive at the tap weights, but $\hat{\mathbf{w}}$ contains the estimate of the filter weights for each channel.

4.9 ALED Analysis

To date, a rigorous mathematical analysis on why the ALED's performance is so robust at low SNRs has yet to be completed and this is an area for future exploration. However, a simple logical argument follows that may give some intuition into the adaptive linear equalizer detector.

Again, at it's core, the ALED is solving the least squares estimate for the optimum

filter tap weights that will undo the channel given by (4.25).

$$\hat{\mathbf{w}} = \boldsymbol{\Phi}^{-1}\mathbf{z} \qquad (4.25)$$

Here again, $\boldsymbol{\Phi}$ is the sample correlation matrix of the received signal and $\mathbf{z}$ is the cross correlation vector between the known signal and the received vector. For very low SNRs (i.e. -20 dB) the sample correlation matrix is approximately an estimate of the noise covariance matrix.

$$\boldsymbol{\Phi} \sim \Re_{vv} \qquad \text{For low SNR} \qquad (4.26)$$

Substituting (4.26) into (4.25) and expanding in terms of the matrix square root yields the following:

$$\hat{\mathbf{w}} = \Re_{\mathbf{vv}}{}^{-1/2}\Re_{\mathbf{vv}}{}^{-1/2}\mathbf{z} \qquad (4.27)$$

Now $\mathbf{z}$ can also be thought of the as the baseband estimate of the channel, $\hat{\mathbf{h}}_{\text{BBCHAN}}$.

$$\hat{\mathbf{w}} = \Re_{\mathbf{vv}}{}^{-1/2}\Re_{\mathbf{vv}}{}^{-1/2}\hat{\mathbf{h}}_{\text{BBCHAN}} \qquad (4.28)$$

Here we can see that the tap weights, $\mathbf{w}$, represents a process that first whitens the baseband channel, then applies a whitened matched channel. If the channel taps are uncorrelated, which is a reasonable assumption, match filtering the channel results in an overall system response of a delta function. This creates the ideal transmission medium which was our intended goal.

Chapter 5

The Experiment

5.1 Introduction

In July of 2011 an acoustic communications experiment was conducted off the coast of Kauai Hawaii (KAM11). Complete details of this experiment are contained in (Hodgkiss and Preisig, 2012) and (Hodgkiss et al., 2011). This chapter will focus on the portions of the experiment that generated the data utilized in testing the adaptive detector.

The data in the experiment was transmitted over two deployments. The deployments occurred from June 25th (JD176) until July 1st (JD182) and July 3rd (JD184) until July 10th (JD191), respectively. During deployment the source WHOI-TX1 transmitted in two hour blocks of time, epochs, and repeated this transmission until retrieval. Epochs begin on even hours. The data for this research was transmitted in minutes 1 to 9 and 61 to 65 of each epoch.

Section 5.2 discusses the locations of the source and receiver deployments. The time-variability of the channel is investigated in Section 5.3. The structure of the transmitted data is discussed in Section 5.4. Finally, Section 5.5 elaborates on why modeling the both the signal and the noise as complex Gaussian random variables is a valid assumption.

5.2 Physical Geometry

The fixed transmitting sources and receiving arrays were deployed along the 100 m isobathymetric curve (see Figure 5-1). The data generated for this thesis was transmitted from source WHOI-Tx1 and received at WHOI-Rx2, stations three and seventeen respectively. The approximate distance between source and receiver is seven kilometers.

The source was deployed to a depth of 15 meters. The top element of the receive array was deployed to a depth 50 meters. The receive array consisted of twenty-four elements with 20 cm spacing ($\lambda/2 \approx 3.75\ kHz$).
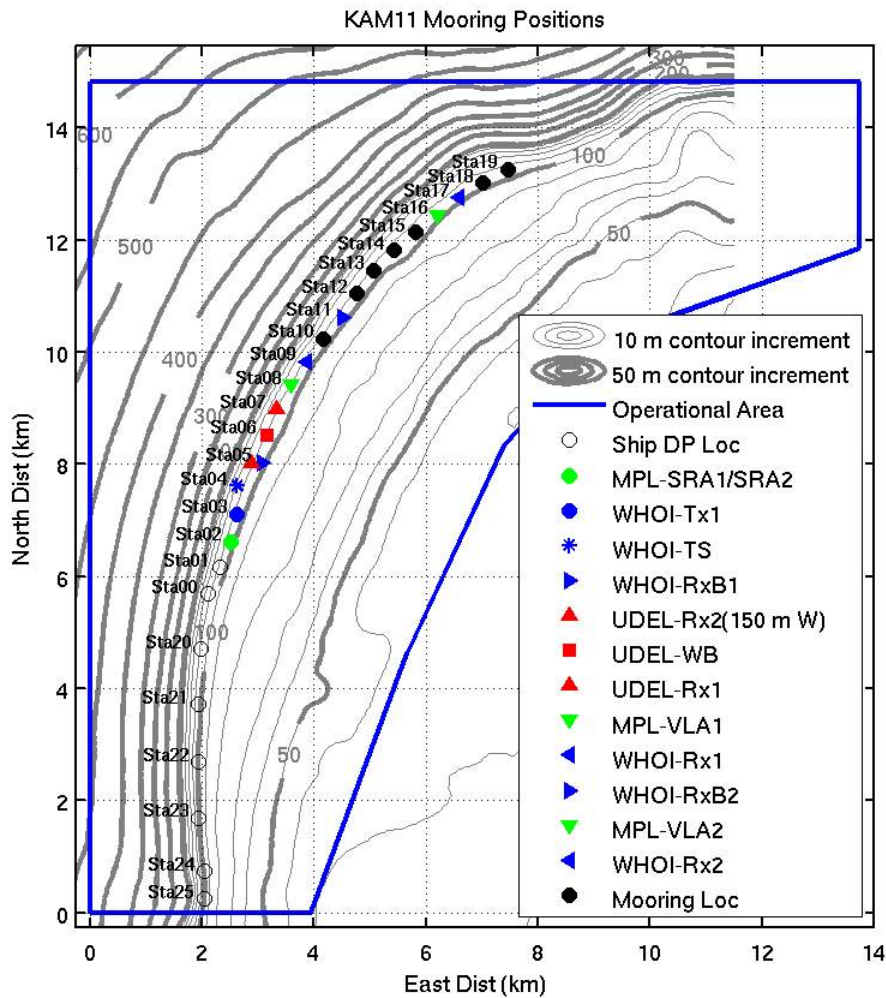

Figure 5-1: This chart contains the mooring positions for the source and receiving array hydrophones. All data processed for this thesis was transmitted by WHOI-Tx1 at STA03 and received at WHOI-Rx2 at STA17.

5.3 Time Variability

The KAM11 experiment took place over several days. During that time the acoustic channel conditions varied significantly due to changing wind and wave conditions as well as tidal changes and internal waves. Figure 5-2 contains wind speed and direction data along with wave spectra, height, direction and intensity for the duration of the experiment.
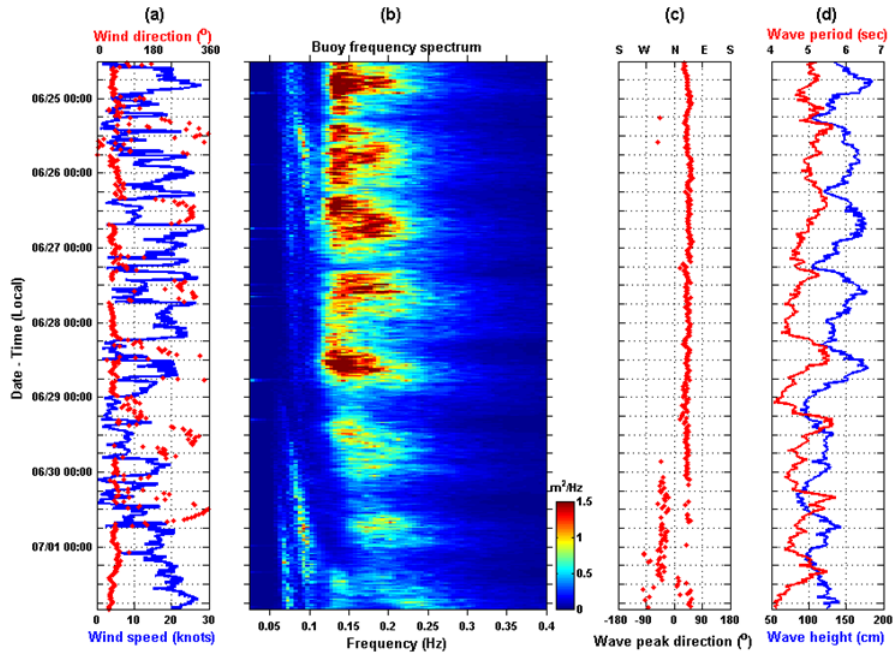

Figure 5-2: This chart captures the environmental conditions during the KAM11 experiment. Plot (a) contains wind speed and direction. Plot (b) contains the frequency spectrum of the surface waves. Plot (c) plots the wave direction. Plot (d) contains the wave period and height.

Figure 5-3 contains seven plots of the estimates of the time-varying channel impulse response between the source and receiver under varying ocean conditions. The plots show the magnitude squared of the channel impulse response as estimated from the received data. Each plot has been normalized to the maximal arrival value that occurred in that file. Ocean conditions varied from high wind and intense choppy surface on JD176 2000z, to calm seas on JD 180 0600z, to moderate wind and ocean swell on JD182 0200z.

Figure 5-3 was generated by conducting a recursive least squares estimate to the
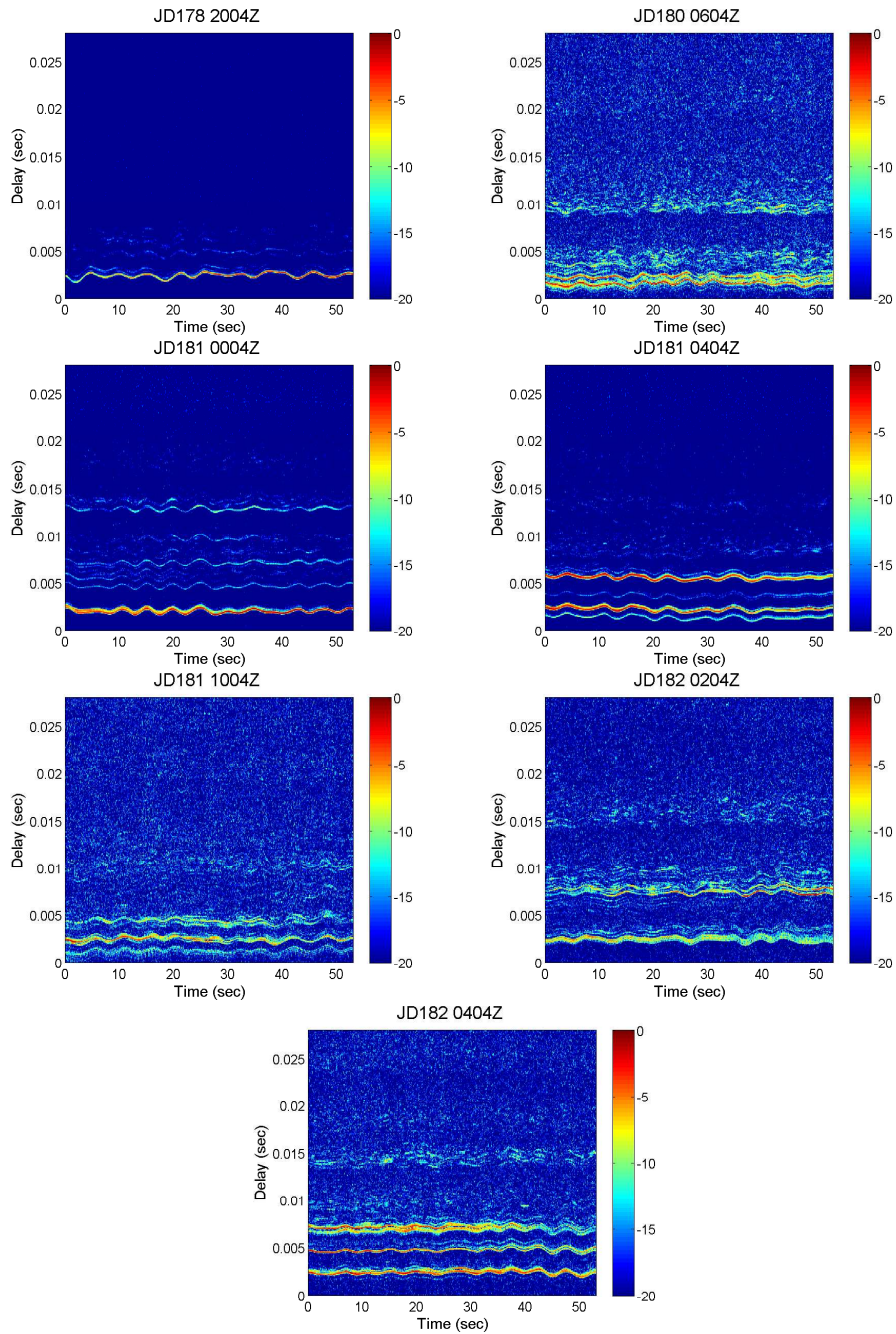
Figure 5-3: Examples of time varying channel impulse responses over 1 minute intervals from source WHOI-TX1 to receive array WHOI-RX2. Environmental conditions varied for each time period for complete description see Wind and Wave chart (NOTE: UTC = Local + 10 hrs).

channel from minutes 3 to 9. Files from these minutes in each epoch contain 81 MLS probes each 4095 symbols in length. All detection files processed by the ED, MF, and ALED were taken from these seven epochs or nearest neighbor epochs.

68

The channel exhibited a large Doppler spread on the main and delayed arrivals of 2 to 4 hertz. Figure 5-4 displays the scattering function estimates and was generated by the methods discussed in Chapter 3.

5.4   Data Structure

The detection sequences are Maximal Length Sequences (MLS), otherwise known as m-sequences. The MLS form was chosen for its high autocorrelation, N for zero lag, and low autocorrelation, 1 for non-zero lag, where N is the length of the sequence. As N approaches infinity the MLS autocorrelation approaches the Kronecker delta function. See Chapter 3 for an example MLS ambiguity function.

In each one minute detection file 16 detection packets were transmitted. Each detection packet consists of a length 127 MLS repeated 30 times for a total data signal length of 3810 symbols.

The transmission signal is a Binary Phase Shift Keyed (BPSK) data signal modulated onto a 13 kilohertz carrier signal. Each symbol contains 16 samples at a sampling rate of 100 kilohertz. The receiver sampling rate was 39062.5 samples per second. Each receive file was resampled to 100000 samples per second and finally downsampled to 2 samples per symbol before being process by the detection algorithms.

5.5   Gaussian Assumption

The derivations for both the energy detector and matched filter were based on a zero-mean complex Gaussian assumption for the noise added at baseband. Additionally, the ED derivation relied on modeling the signal as a complex Gaussian random variable. To verify these assumptions histograms were generated for the pure noise files (minutes 83 and 84) and the signal plus noise files (minutes 61 to 65) in each epoch. Additionally, the MATLAB function *normfit.m* was used to estimate the equivalent Gaussian probability density function for each file.

The histograms and Gaussian estimates for the noise files are demonstrated in Figure 5-5. The figure is an example from JD178 2183z. The remaining noise files were processed (not shown here) and exhibit similar Gaussian statistics. It is apparent from Figure 5-5 that the noise is complex circular Gaussian.

The signal plus noise file histograms are displayed in Figure 5-6. Again, these files are well modeled by complex circular Gaussian random variables. The histograms of the signal plus noise files represent an estimate of the convolution of the signal pdf and the noise pdf. Additionally, the convolution of two Gaussian probability density function is also Gaussian. Therefore by demonstrating that the noise and the signal plus noise PDFs are Gaussian, it is reasonable to assert that the signal can also be modeled as a complex circular Gaussian random variable.

(a) JD178 2000Z

(b) JD180 0600Z

(c) JD181 0000Z

(d) JD181 0400Z

(e) JD181 1000Z
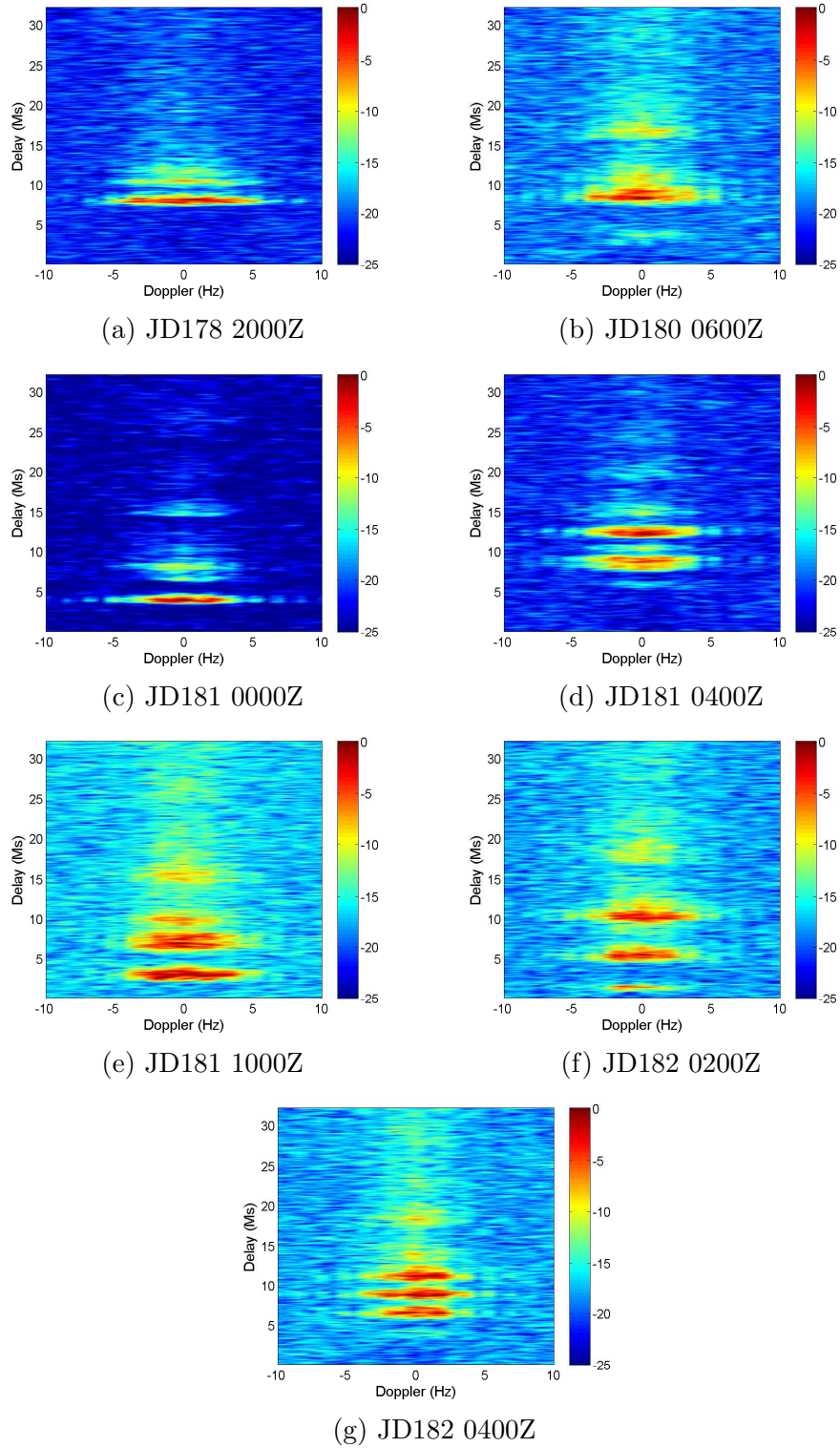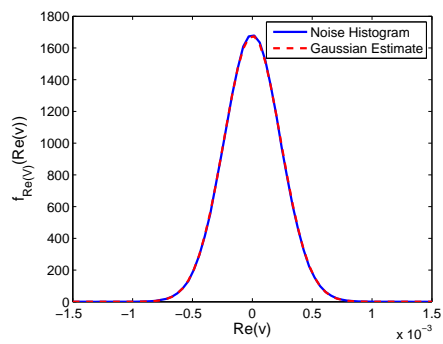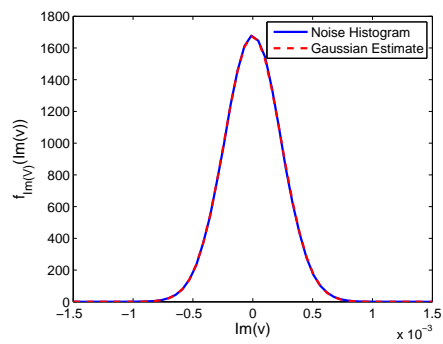
(f) JD182 0200Z

(g) JD182 0400Z

Figure 5-4: Scattering function estimates for the canonical epochs generated from MLS probes in minutes 3 to 9 of each epoch. Environmental conditions varied for each time period for complete description see Wind and Wave chart (NOTE: UTC = Local + 10 hrs).
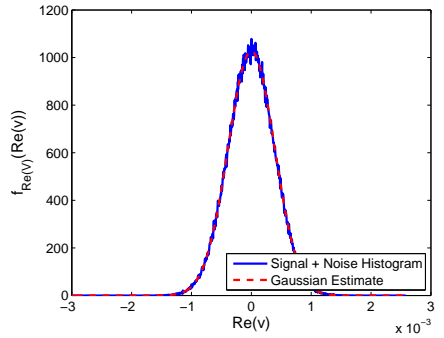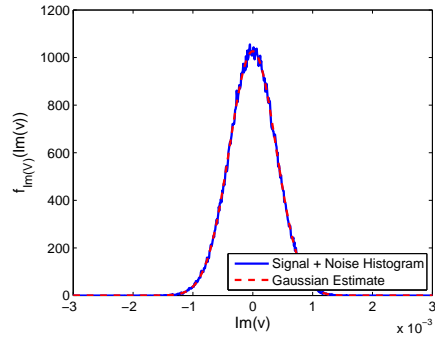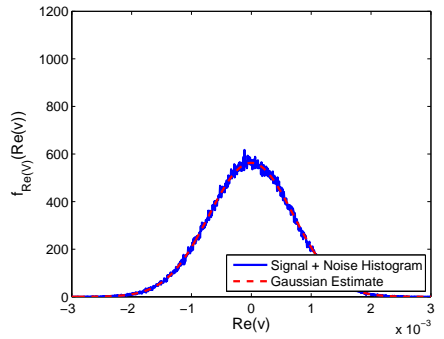
(a) JD178 2123z   (b) JD178 2123z

Figure 5-5: Examples of noise histograms with Gaussian estimates. The left column contains estimates from the real portion of the file while the right column contains the imaginary portion. The noise files were generated from minute 83. It is apparent from these plots that the complex circular Gaussian assumption is valid for the additive noise.
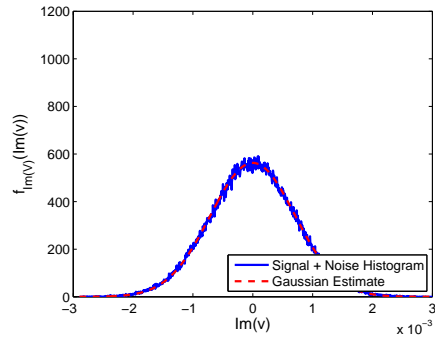
(a) JD178 2000z $SNR \sim 0$ dB   (b) JD178 2000z $SNR \sim 0$ dB

(c) JD180 0600z $SNR \sim 8$ dB   (d) JD180 0600z $SNR \sim 8$ dB
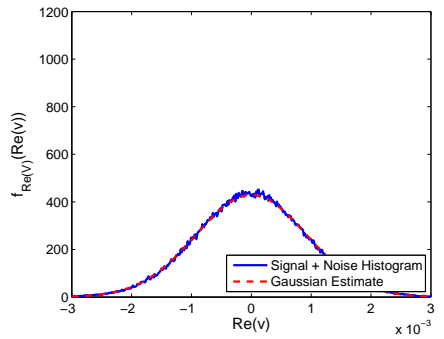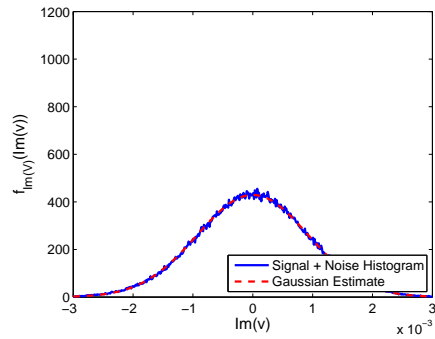
(e) JD182 0200z $SNR \sim 12$ dB   (f) JD182 0200z $SNR \sim 12$ dB

Figure 5-6: Examples of signal plus noise file histograms with Gaussian estimates. The left column contains estimates from the real portion of the files while the right column contains the imaginary portion. The signal plus noise files were generated from minutes 61 to 65 from the respective epochs. It is apparent from these plots that the complex circular Gaussian assumption is a valid model for the signal.

Chapter 6

Results

6.1   Introduction

This chapter discusses the results of each detector applied to the KAM11 experimental data. The MF's and ED's performance will be compared to theoretical analysis and a Monte Carlo simulation. In the case of the ALED, each control parameter is analyzed to determine the optimum set of characteristics for the KAM11 channel.

In Section 6.2, the method by which all files are processed prior to implementing the desired detector is discussed. Section 6.3 introduces channel modeling issues. The Monte Carlo simulations used in this thesis are explained in Section 6.4. The single array element ED and MF results are presented in Sections 6.5 and 6.6, respectively. Section 6.7 discusses beamforming the receive array to improve detector performance. Finally, Section 6.8 discusses the results for the proposed adaptive detector and compares these to the beamformed MF.

6.2   Received Signal Processing

Each received file has a sampling rate of 39062.5 samples per second. First, each file is resampled to a sampling rate of 100000 samples per second. Resampling resets the samples per symbol to 16, an integer whole number. The signal is then brought to baseband. The baseband signal is filtered with a low pass filter to remove the

unwanted portions of the frequency spectrum. The low pass filter is a 42ND order equiripple filter with a passband region from 0 to 5000 Hz. The stopband is attenuated to -50 dB and begins at 9000 Hz. After the baseband signal is filtered, it is downsampled to 2 samples per symbol.

The native SNR in the files processed by this thesis ranges from 0 dB to 12 dB. However the purpose of the ALED is to demonstrate reliable signal detection and synchronization at much lower signal to noise ratios. To reduce the SNR in each file, first the native SNR is calculated to determine the additional noise required. Then a scaled, basebanded, filtered, and downsampled version of file 83, a noise only file from the corresponding epoch, is added to the baseband signal file to achieve the desired SNR. The downsampled signal plus noise file is then sent to the ED, MF or ALED for further processing.

6.3   The KAM11 Channel

The ocean channel for the transmitted data in this thesis has not yet been extensively studied and therefore not fully implemented in the Monte Carlo simulations. For the MF and ED, the Monte Carlo simulation was initially implemented with an ideal channel and compared to the theoretical predictions. Then a simple channel model was implemented in simulation to introduce channel coherence issues.

6.4   Monte Carlo Simulation

In the Monte Carlo simulation, every effort was made to process the data in the exact manner as the KAM11 data. Each simulation was started with the actual passband signal used in the KAM11 experiment. As was mentioned in Chapter 5 each file contains 16 detection signal transmissions. The simulation processed 65 files to get statistically significant number of detection locations. This is the same number of files used when processing the KAM11 data.

The signal was brought to baseband and passed through a low pass filter. The

same filter was used when processing the actual KAM11 data. The signal was then passed through a baseband channel, initially through an ideal channel to verify the simulation against the theoretical performance, and ultimately through one of two simple channel models: a Doppler shifted channel or an auto-regressive channel model. Each model uses a single tap channel to investigate the effect of temporal fluctuations on the performance of the detectors. The Doppler shifted channel is given by (6.1).

$$g[n] = e^{-j2\pi \frac{f_{\mathrm{D}}}{f_{\mathrm{S}}} n} \tag{6.1}$$

Here, f_{D} is an unknown Doppler shift in Hertz of the channel and f_{S} is the sampling frequency of the received signal. The second model was a single tap auto-regressive channel. The equation for the tap is given by (6.2).

$$g[n+1] = \alpha g[n] + v[n] \tag{6.2}$$

Here, α controls the correlation time of the channel and $v[n]$ is zero-mean white complex Gaussian process noise. These two channels were used to demonstrate the reduction in performance of the MF due to channel incoherence. After the channel was applied, complex Gaussian white noise was added to degrade the received signal to the desired SNR. Finally the appropriate detector was applied to the simulated received signal.

6.5   Energy Detector Results

The clairvoyant ED knows the signal bandwidth and transmission duration of the detection pulse. As mentioned in Chapter 5 the detection sequence is 3810 symbols long at a transmission rate of 6250 symbols per second. This gives the ED an integration interval (or summation in discrete terms) of approximately 0.6 seconds. The energy detector is not susceptible to coherence issues like the matched filter so the Monte Carlo simulation for the ED made an ideal channel assumption.

Figure 6-1 compares the theoretical results from Chapter 2 to the ED Monte Carlo

simulation. It is apparent from these figures that they are in good agreement. Note, for an energy detector of this length, even at -10 dB SNR, it is theoretically possible to achieve perfect detection. Figure 6-2 contains the results from applying the ED to the KAM11 data. Here it is apparent that the ED is not performing up to its theoretical potential. The ED on the KAM11 data at -10 dB does far worse than the predicted perfect detection and at -20 dB, the ED ROC is essentially diagonal which corresponds to the ED flipping a coin to determine if the signal is present. Further research is required to determine why the KAM11 channel is having this detrimental effect on the ED.
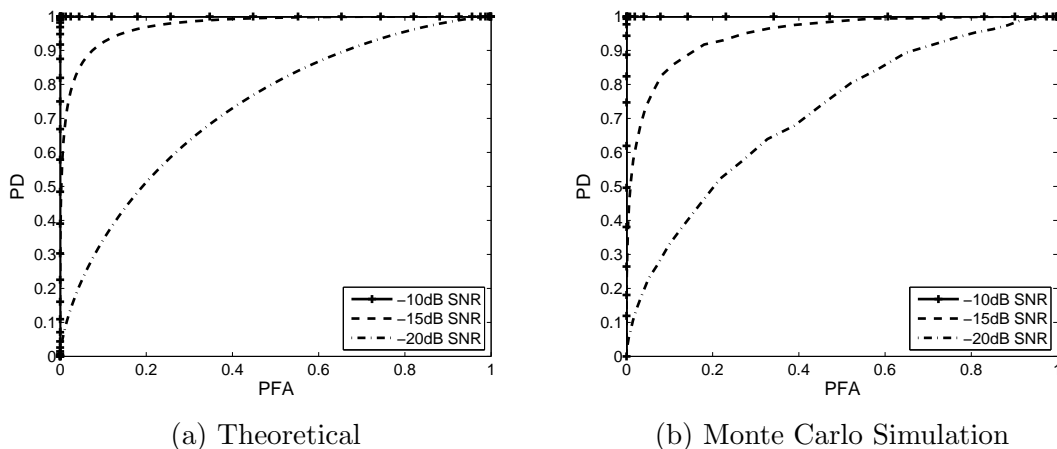

(a) Theoretical   (b) Monte Carlo Simulation

Figure 6-1: Theorectial versus Monte Carlo simulated ED ROC for $N = 7620$.

6.6 Matched Filter Results

In Chapter 3 it was determined that the matched filter gain was proportional to its length for the ideal channel. Probability density functions were calculated and theoretical ROC plots were generated. Here we will compare the theoretical results to the Monte Carlo simulation done with an ideal channel assumption. As mentioned earlier, there are 3810 symbols in the detection sequence. In a fully coherent channel the MF can take advantage of the full signal transmission length. However it is not instructive to look at the ideal channel results for a MF of this length since at the desired SNR it achieves perfect detection. So for the initial comparison between
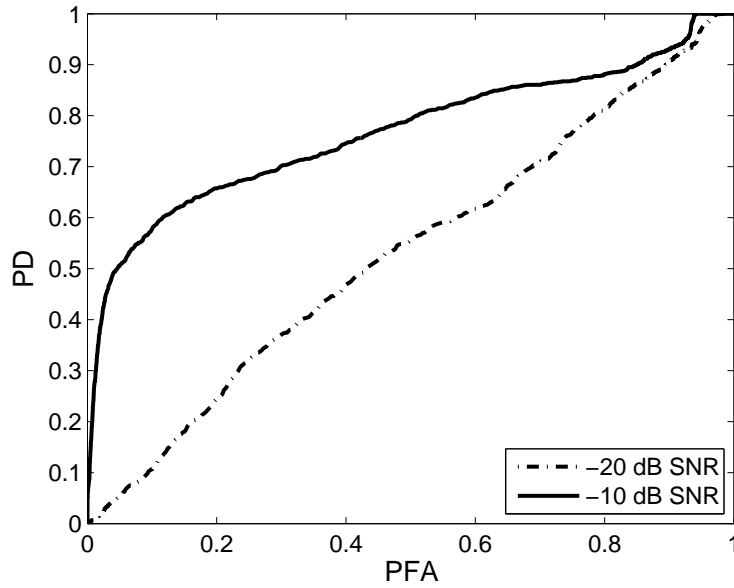
Figure 6-2: An ED of sample length 7620 applied to the KAM11 data over 1040 detection regions.

theory and simulation the MF length will be kept to one MLS with a length of 127 symbols. This comparison is displayed in Figure 6-3. Again, for the ideal channel, there is good agreement between predicted and theory. However, there is some minor performance degradation in the simulation. This can be possibly attributed to limited sample size of 1040 detection regions in the simulation.
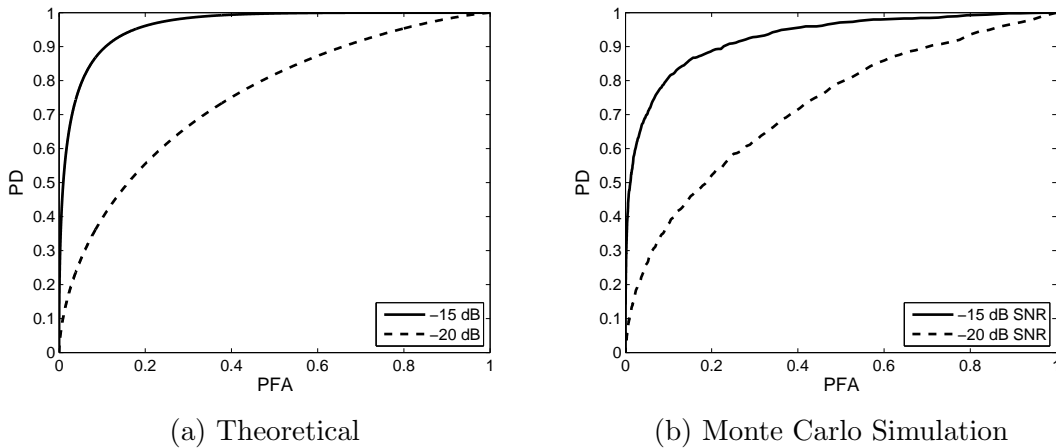

(a) Theoretical

(b) Monte Carlo Simulation

Figure 6-3: Theorectial versus Monte Carlo simulated MF ROC for $N = 127$.

Next it is useful to look at how coherence length can effect the MF. As discussed

in Section 6.4 we will use two models: the Doppler shift and the auto-regressive tap. The Doppler shifted model was applied with a 1.7 hertz Doppler shift. For the auto-regressive model, α was chosen to be 0.9995. This α gives the tap weight a 10 percent auto-correlation of 3700 samples, or 1850 symbols. The expected output SNR of the MF as a function of the MF length is plotted for both models in Figure 6-4.

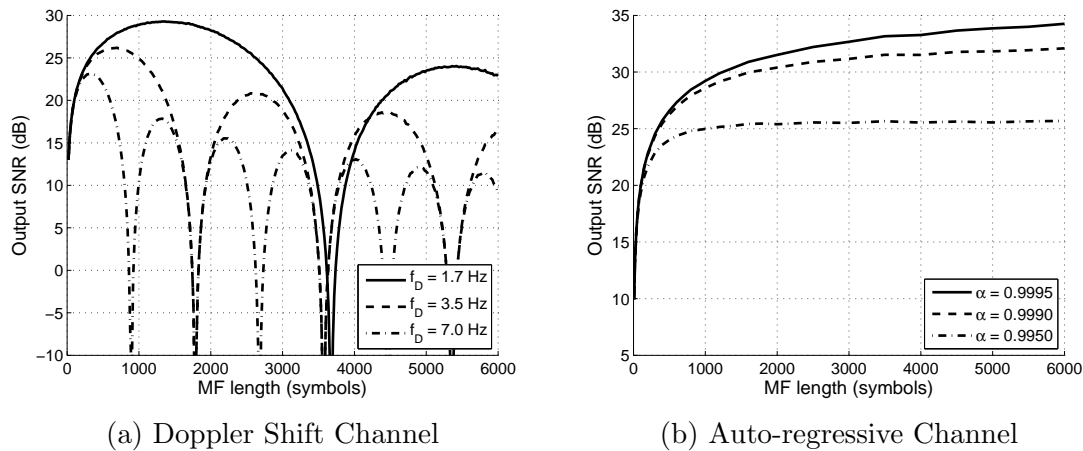(a) Doppler Shift Channel   (b) Auto-regressive Channel

Figure 6-4: MF output SNR as a function of MF length for a Doppler shifted channel and a single tap auto-regressive channel.

From Figure 6-4 it is apparent that both models affect the performance of the MF. However, in the Doppler shifted model destructive interference is occurring which actually lowers the performance of the MF when the length exceeds the peak of the first lobe. For a Doppler shift of 1.7 Hz this is approximately 1300 symbols. In the auto-regressive channel, we can see that the MF gain asymptotically approaches a limit. For an α of 0.995, this limit is reached at approximately 1200 symbols. A MF longer than this length provides no additional benefit, but the gain is also not reduced.

Both channels were used in simulation and various length MFs were applied to the simulated received signal. Figure 6-5 plots the ROC curves for each MF length. You can clearly see from this figure that the channel generated from the Doppler shifted model reduces the effectiveness of the MF. From Figure 6-4 we expected maximum performance of the MF near 1300 symbols, the best performing MF for the Doppler shifted channel was 1270 symbols in length. It is also interesting to note that a MF

length of 127 performed close to the theoretical prediction displayed in Figure 6-3, but as the length increased to 3175 the filter performed worse than its far shorter counterpart. These results are consistent with the discussion of the Doppler shifted channel in Chapter 3.

In the auto-regressive channel we also see performance degradation, but notice continued improvement as the filter length gets longer. This performance is consistent with our expectations based on Figure 6-4.

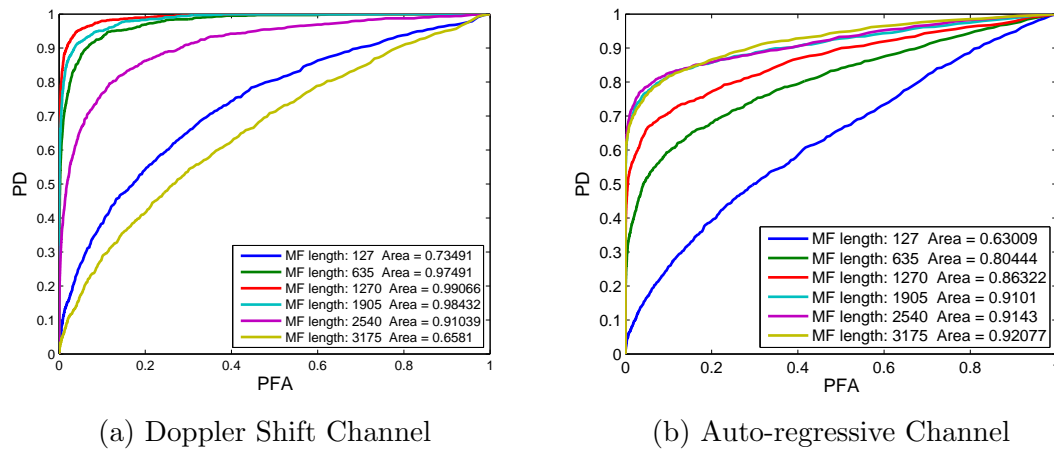(a) Doppler Shift Channel   (b) Auto-regressive Channel

Figure 6-5: The plot depicts a MF applied to a Doppler shifted channel Monte Carlo simulation and a single tap auto-regressive channel Monte Carlo simulation at -20 dB SNR. Various symbol length filters were applied.

From the scattering function figures in Chapter 5 we saw the main arrival in each epoch contained a Doppler spread of 3 to 8 hertz. A Doppler spread is not as detrimental to the MF as a pure unknown Doppler shift. This is because for a portion of the time there is zero, or a very small, Doppler shift and the MF will perform better during those times. Additionally, a simple unknown Doppler shift does not simulate the other random effects of the channel or the multipath arrival structure.

Figure 6-6 shows the results from the MF applied to the actual data. In this figure we can see that the MF achieves some improvement as the length increases up to 1800 symbols, but sees decreased performance returns for longer filters. We have applied two simple channel models and have seen that neither fully describes the effects of the KAM11 channel. The overall performance degradation is better modeled by the

auto-regressive model, but the KAM11 channel exhibits similar losses to a Doppler shift when the MF length is longer than the coherence length of the channel.
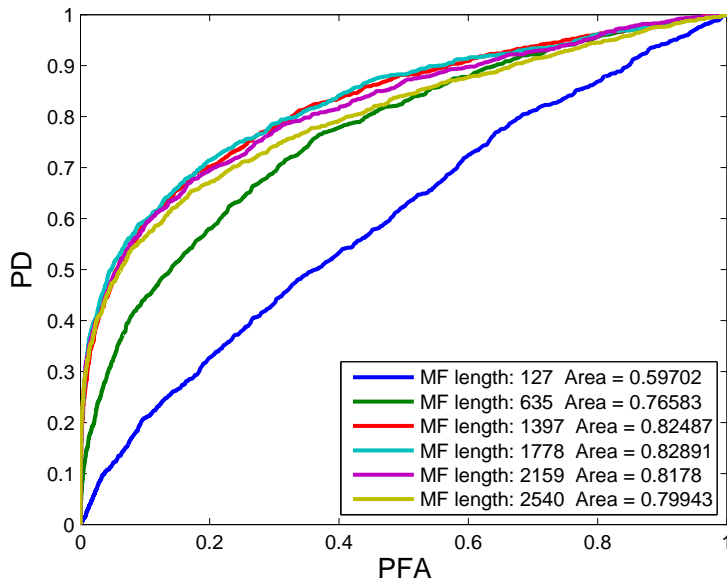

Figure 6-6: The plot depicts a MF applied to 1040 KAM11 detection locations at -20 dB SNR. Various symbol length filters were applied and the filter demonstrated maximum performance for a length near 1800 symbols.

6.7 Beamforming

The ALED has the ability to use all 24 elements of the array without beamforming the signal prior to processing. For both the ED and the MF to this point, we have assumed only one element was available for processing and the results thus far have been from element 1 on the array. For the ED and MF to take full advantage of the array requires knowledge of the direction from which the signals are coming. In the KAM11 experiment we are utilizing a 24 element vertical array, beamforming that array to broadside to look for the signal is a logical choice, however in an actual detection scheme the beam would need to swept across all possible arrival angles.

It is important to note that the array is not ideally spaced for the center frequency in use. The carrier is transmitted at 13 kHz, while the array element spacing is 20 cm ($\lambda_{\text{Fc}}/2$ for 3.75 kHz). The end result is interfering grating lobes at approximately

82

40 degrees off of broadside. The spatial structure of the noise only files (minutes 83 and 84 of each epoch) and the spatial structure of the signal plus noise files were investigated. The expectation after this review was that beamforming to broadside should improve the performance of both detectors. The spatial structure with an overlaid broadside beam is shown in Figure 6-7. The noise energy is flatter across angle space than the signal, as would be expected, but it appears more noise energy is coming from broadside than other directions.

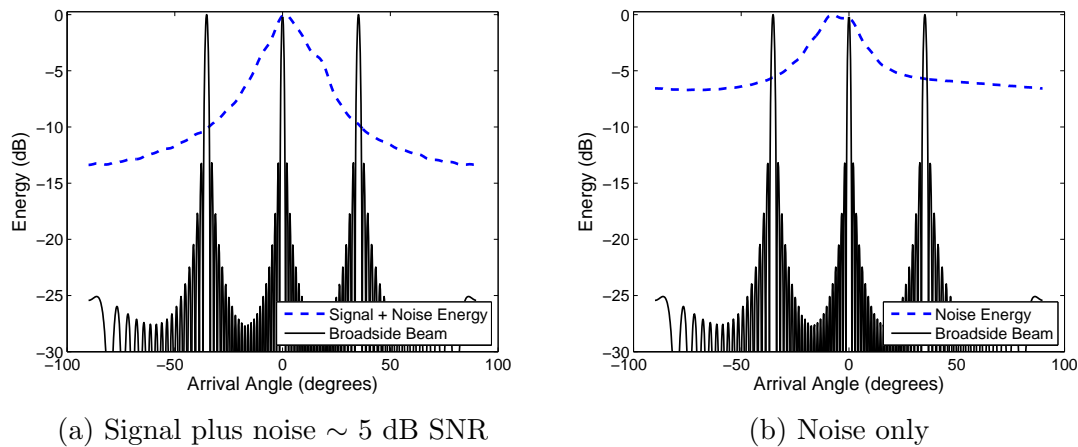(a) Signal plus noise $\sim$ 5 dB SNR   (b) Noise only

Figure 6-7: The signal plus noise plot was generated from an average completed over 65 transmission files, SNR varied from 0 dB to 12 dB. The noise only plot was generated from minute 83 in each of the corresponding epochs. A broadside beam has been overlaid, notice the grating lobes due to the element spacing of 20 cm.

An alternative choice to beamforming, that still uses all 24 elements, is using a ED or MF on each element and incoherently summing the outputs. Since each element, standing alone, is omni-directional, knowledge of the signal arrival direction is not required. Both of these methods were tried for the ED and MF and ROC curves were generated for both in Figure 6-8.

The MF processed on the beamformed array does display a marked improvement, however the ED did not see the same increased performance. The incoherent sum of elements, for both MF and ED, did not show any performance improvement over the single element's performance. Note: the ED ROC curves were generated at -10 dB due to its poor performance at lower SNRs. The ALED will compared to the broadside beamformed MF.

83

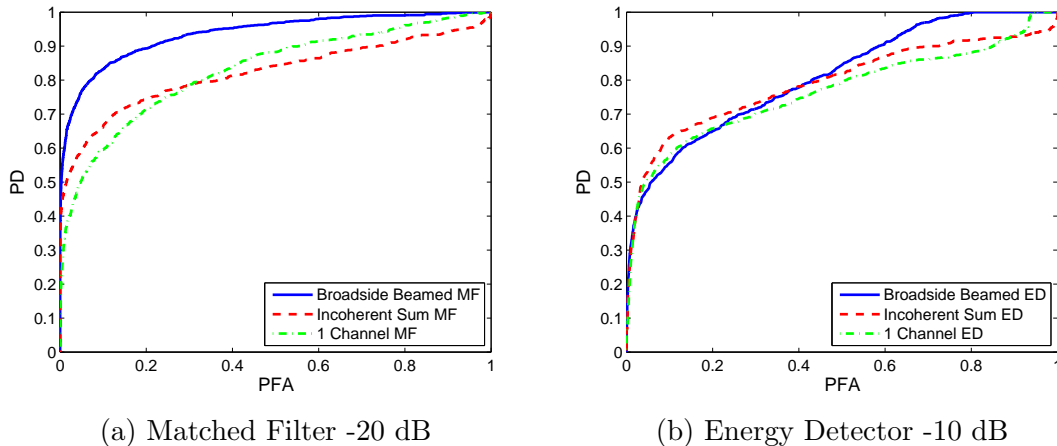(a) Matched Filter -20 dB   (b) Energy Detector -10 dB

Figure 6-8: Broadside beamformed, incoherent average and 1 element results for the MF and ED using KAM11 received signals. The MF is displayed for -20 dB and the ED is displayed for $-10 \quad dB$.

6.8   ALED Detector Results

Unlike the MF and ED, the ALED has more than one parameter controlling its performance. This thesis evaluates the following parameters: M is the temporal length of the equalizer's feedforward filter expressed as number of symbols, λ the RLS forgetting factor, a soft decision averaging length, and λ_{BER} the BER window exponential weighting. Additionally, as described in Chapter 5, the receive array consists of 24 hydrophones, making 24 receive channels available. This thesis compares the results of three different ALED structures that trade off the balance between pure temporal processing and spatial and temporal processing combined.

The three ALED structures are: 24 one channel equalizers whose outputs are averaged into one soft decision, 4 six channel equalizers whose outputs are averaged into one soft decision, and finally 1 twenty-four channel equalizer. The trade offs are as follows, the twenty four channel equalizer estimates the full time-space-average correlation matrix, but these matrices are large and results in an additional computational cost. Furthermore, there is a trade off in dimensionality, SNR, and rate of channel fluctuation. As the SNR falls, the dimensionality of the estimate must decrease or the averaging time must increase. However, the averaging time is limited by the rate of channel fluctuation. Often, in a rapidly fluctuating channel, reducing

84

the dimensionality of the problem is the only option which improves performance.

On the other extreme we have 24 one channel equalizers. Each channel's equalizer is responsible for estimating the time-average correlation matrix. The outputs from each equalizer are then averaged into one soft decision. The optimum method for combining these soft decisions is an area that requires more study, but a simple mean value was used in this thesis. This equalizer structure essentially throws out the spatial cross-correlations and only estimates the temporal diagonal region of the time-space-average correlation matrix. This reduced dimensional problem is the fastest computationally.

The third structure attempts to strike a balance between the other two. It uses 4 six channel equalizers and the outputs are averaged into one soft decision. The 24 channels are split into four sub-arrays each consisting of six elements spaced four elements apart i.e. equalizer one uses elements in the set $[1, 5, 9, 13, 17, 21]$, equalizer two uses $[2, 6, 10, 14, 18, 22]$ and so on. This scheme captures some of the spatial correlations, but does not estimate the full correlation matrix. It has the ability to benefit from increased information but is not as computationally expensive as the twenty-four channel equalizer, and less likely to become ill conditioned as the SNR falls.

Initially several investigations in to the ALED performance were conducted in anticipation of utilizing a structure combining sets of eight elements. It later became apparent during testing that combining four sets of six elements performed well. The lessons learned from testing the eight channel equalizer were utilized in setting the parameters for the six channel equalizers.

To simplify notation the following are equivalent:

- 1 one channel equalizer = 1X1
- 1 eight channel equalizer = 1X8
- 4 six channel equalizers = 4X6
- 24 one channel equalizers = 24X1
- 1 twenty-four channel equalizer = 1X24

6.8.1 Filter Length

All three schemes were operated at a fractional spacing of two, or two samples per symbol. This is the same symbol spacing used in both the MF and the ED. With a fractional spacing of two, this corresponds to a filter length of $2M$, where M is the number of symbols in the equalizer. For example, a six channel equalizer has a sample space-time correlation matrix that is $12M$ by $12M$.

The time-delay figures in Chapter 5 reveal strong secondary arrivals up to 5 ms after the main arrival. This time spread equates to around 30 symbols. It seams logical that having the equalizer filter span all of the delayed arrival peaks would be beneficial. To test this, minute 4 from each epoch was processed, using over 125000 transmitted symbols, and the BER was calculated. Initially three different equalizer channel combinations were tested: 24X1, 1X24, and 1X8. Each combination was tested over a range on M values. Due to the computational expense of the 1X24, M was limited to 10.

Figure 6-9 plots the three equalizer's performances versus filter length (in symbols). It is instructive to compare Figures 6-9 and 5-3. In epochs with strong second arrivals it appears useful for the equalizer to attempt to span both arrivals to gain improved performance. Additionally, the 1X8 and 1X24 curves, which attempt to use more spatial information tend to turn up sooner and the added information from the second arrival cannot offset the increased adaptation noise in the filter.

The results of all seven epochs were averaged to determine an optimum filter length over varying conditions. This is shown in Figure 6-10. The results were revealing. The more spatial processing the equalizer attempted, the sooner the BER increased with filter length. There appears to be two competing effects taking place. Each equalizer in the 24X1 is omni-directional. As the number of array elements in each equalizer increases, more spatial processing occurs allowing the equalizer to remove interfering late arrivals. However, the dimensionality of the adaptation problem rises much quicker in the equalizers utilizing more array elements as the number of temporal taps in each channel increases. This causes the adaptation error to increase more rapidly,
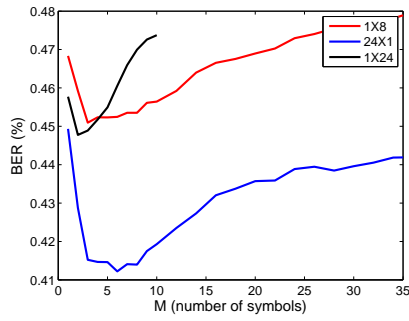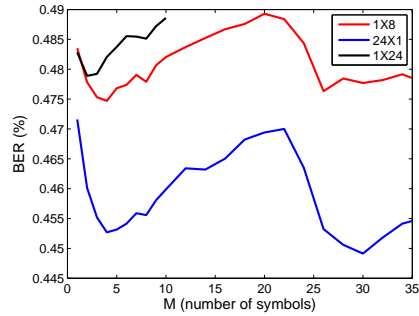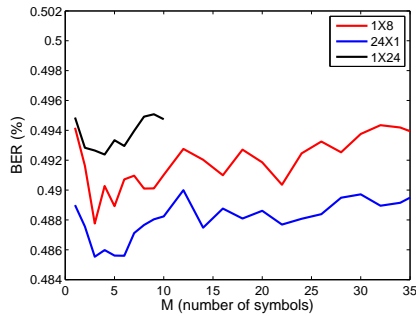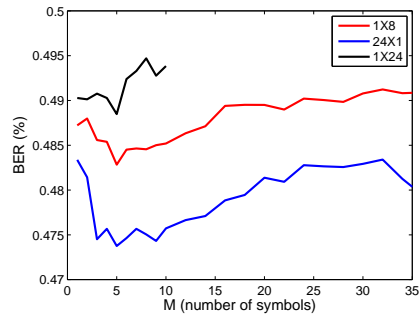
(a) JD178 2000z
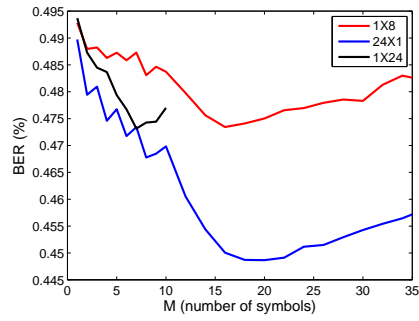
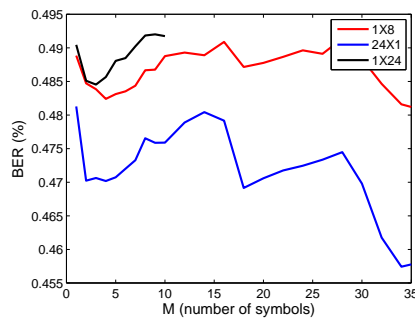(b) JD180 0600z
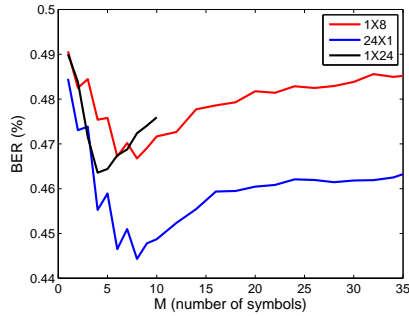
(c) JD181 0000z

(d) JD181 0400z

(e) JD181 1000z

(f) JD182 0200z

(g) JD182 0400z

Figure 6-9: Equalizer BER performance for filter lengths spanning M symbols. Three styles are compared: 24X1, 1X8, and 1X24 channel. The 1X24 channel was only examined up to 10 symbols due to computation cost.

as a function of temporal length, in the equalizers that utilize spatial processing.

With these findings it was determined to test the ALED with symbol lengths of 5 and 10 for comparison. Note: the bit error rates in Figures 6-10 and 6-9 are not representative of what the ALED can achieve, but a measure of the individual soft decision quality prior to any further processing.

Figure 6-10: Equalizer BER performance for filter lengths spanning M symbols. Three styles are compared: 24X1, 1X8, and 1X24 channel. The 1X24 channel was only examined up to 10 symbols due to computation cost.

6.8.2 Forgetting Factor

The next parameter investigated was the forgetting factor λ. The forgetting factor is a measure of the memory in the equalizer. A good rule of thumb is setting $\frac{1}{1-\lambda}$ much much less than the coherence length of the channel.

Earlier we saw the MF detector saw no improvement past filter length of ~ 2000. Using 2000 symbols as an estimate of the correlation length puts an initial guess for λ at 0.995, which corresponds to an approximate memory length of 200 symbols. A range of values around this initial λ estimate were tested. Values were limited to the set $[0.999, 0.998, 0.995, 0.993, 0.99]$, which equates to a memory range from 100 to

1000 symbols.

(a) 1X8

(b) 24X1

(c) 1X24
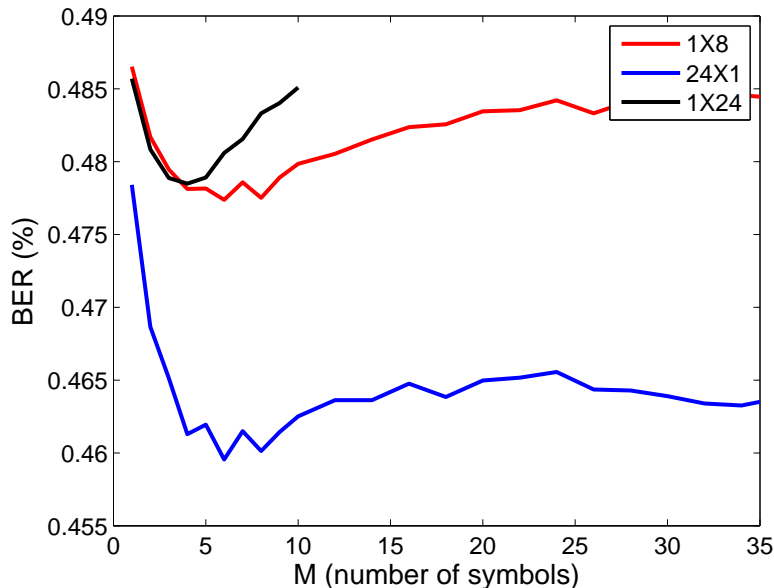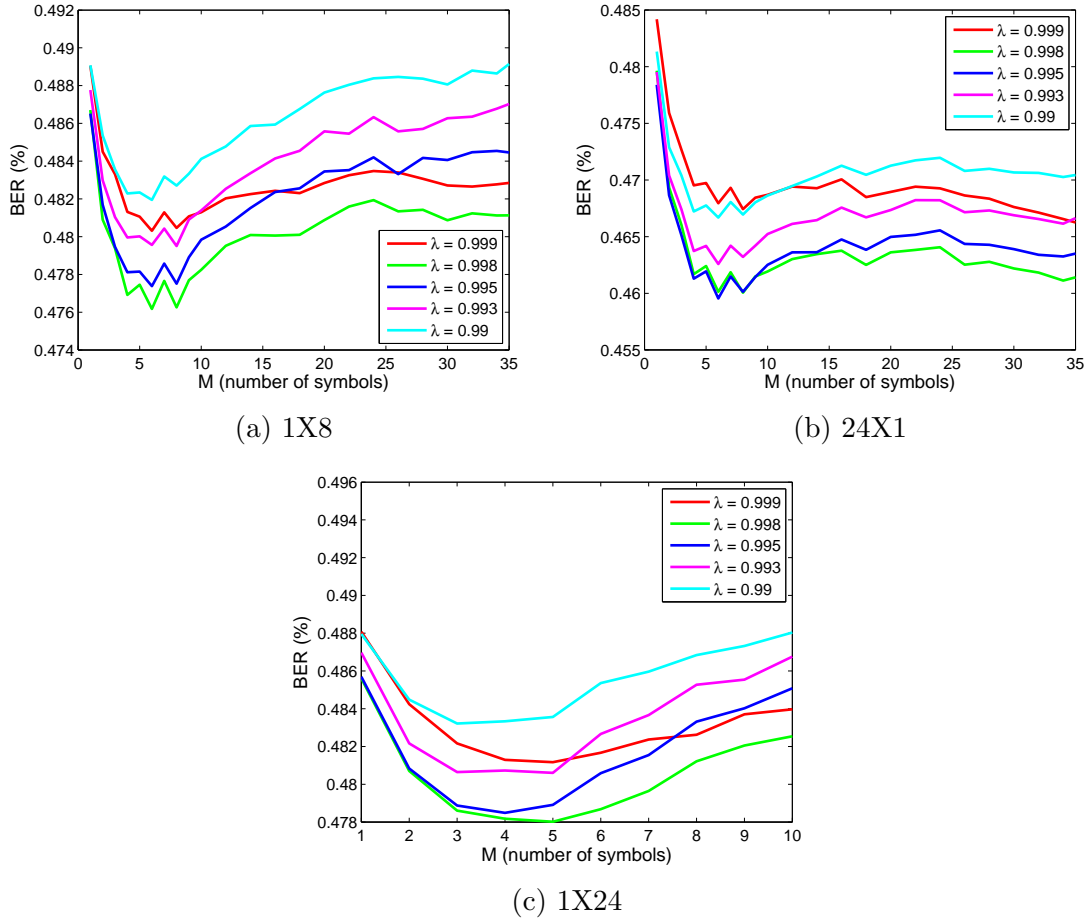
Figure 6-11: Equalizer BER performance for filter lengths spanning M symbols. Three styles are compared: 24X1, 1X8, and 1X24 channel with various forgetting factors. The 1X24 channel was only examined up to 10 symbols due to computation cost.

By inspecting Figure 6-11 we can determine a few attributes of λ:

- A forgetting factor less than 0.995 appears to be too short an averaging window for this channel.

- The 24X1 is estimating the smallest portion of the correlation matrix and has the shortest averaging window that performs well.

- As the number of taps in the filter increases, each equalizer has more noise to average out, and the relative performance of the longer averaging windows improves.

Based on Figure 6-11 forgetting factors of 0.995 and 0.998 were chosen as testing parameters for the ALED.

6.8.3 Soft Decision Averaging

As discussed in Section 4.7.2 using more than one soft decision to make our hard decision could improve our estimate. The detection signal is 3810 symbols long. It consists of 30 repeated m-sequences, each 127 symbols long. A simple averaging scheme would take soft decisions spaced out 127 symbols in time and averaging them prior to making the hard decision. Since the signal is repeated with a period of 127 symbols each of these soft decisions will be estimating the same symbol. The delay introduced is $S \times 127$ where S is the number of desired soft decisions to average. With this spacing, S is limited to a maximum value of 30.

Since the transmitted detection signal is a BPSK MLS, other possible soft decision combinations are available. For instance, every tenth soft decision could be averaged by first multiplying each soft decision by its appropriate coefficient, 1 or -1. This would allow averaging 381 soft decisions together reducing the variance of the estimate below the 127 symbol spacing. However there are trade-offs to using this many soft decisions. The symbol estimates at time n and time $n + 1$ will be uncorrelated but, the estimates at time n and $n + 10$ will be highly correlated since they have 380 soft decisions in common. This scheme would only give 10 uncorrelated symbol estimates from which to generate a BER, where as the previous scheme has 127. The ALED was tested with the 127 symbol spacing for $S = 5, 10, 18, 25$, and 28. Figure 6-12 displays the results. The ALED achieved its highest P_{D} for $P_{\mathrm{FA}} \leq 10^{-6}$ when 25 soft decisions were averaged.

It seems counter intuitive that averaging 25 soft decisions would outperform an average over 28 soft decisions. However, in utilizing 28 soft decisions we have narrowed the window from which we can estimate our BER to 381 symbols. This narrow window leaves little time for the equalizer tap weights to converge to an adequate filter estimate. Using only 25 soft decisions doubles number of symbols in our BER estimate while still using a large number of soft decisions to reduce the variance in
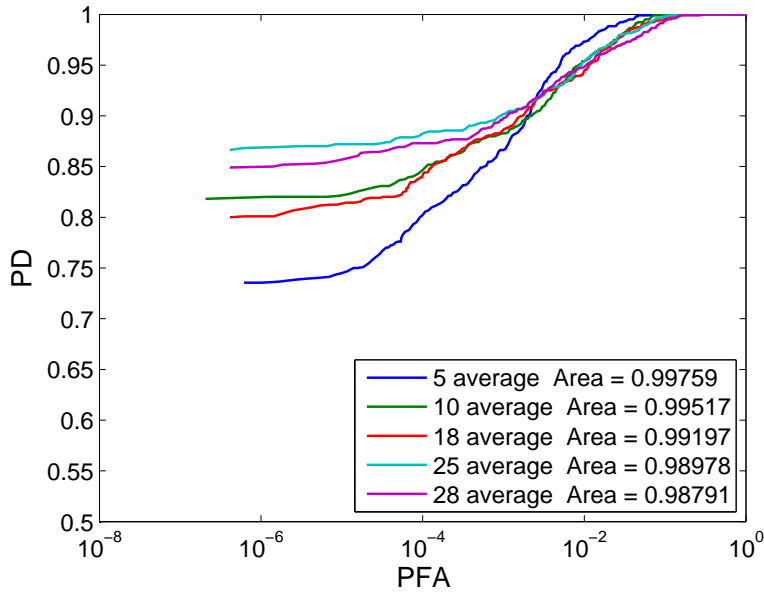
our symbol estimates.

Figure 6-12: The 4X6 ALED was tested with varied soft decision symbol averaging using 5, 10, 18, 25, and 28 soft decisions in the average. Each soft decision was spaced out 127 symbols in time.

6.8.4 BER window

The BER window is an exponentially weighted running BER calculation. The adjustable parameter λ_{BER} sets the length of the window. The BER calculation is given by (4.19), where λ_{BER} takes values between 0 and 1. Longer values smooth out the BER calculation which reduces false alarms. However, in trade, the BER takes longer to converge to the true instantaneous value causing possible missed detections. The ALED was tested for λ_{BER} in the set $[0.9995, 0.999, 0.9985, 0.9975, 0.995]$.

Figure 6-13 compares ROCs generated with different BER windows for two different ALED configurations, a 24X1 with 10 taps and a 4X6 with 5 taps. Both different configurations achieved their highest performance when $\lambda_{\text{BER}} = 0.999$. Here, we have assumed the criteria for highest performance is the highest P_{D} for a $P_{\text{FA}} \leq 10^{-6}$.

Other metrics could have been used, in fact the shortest duration BER window achieved the largest area under the ROC in both configurations. If the criteria had

been $P_{\text{FA}} \leq 10^{-4}$, $\lambda_{\text{BER}} = 0.995$ would have been chosen. In either case, the ALED performed well over the range of values indicating a tolerance to error in the optimum exponential weighting of the BER calculation.

6.8.5   BER decision combining

Based on the detection symbol structure of 30 repeated m-sequences of length 127, the ALED is running 127 parallel equalizers. Each of these equalizers are estimating the current symbol and tracking a windowed BER. There are several possible methods by which a detection could be flagged. In one possible scheme the ALED could flag a detection if any, in the bank of BERs, fell below the threshold. Another could flag a detection when the average of the lowest three (four, five, etc...) drop below the threshold.

Nearby equalizers (one or two symbols off synchronization) will perform nearly as well as the synchronized equalizer. As long as they span the majority of the main arrival the equalizer will be able to undue the channel effects where a longer or shorter delay has been assumed. Based on this premise, another combining scheme presents itself, using the average lowest contiguous three (four, five, etc...) BERs. When the ALED is on the signal the equalizers with the next lowest BERs should be nearby. When the ALED is receiving noise only, the lowest BERs should be randomly spread over all the parallel equalizers. The thought is that using the average of contiguous equalizers will reduce false detections. The ALED was tested with the contiguous method, averaging over five equalizers.

6.8.6   ALED Performance Results

In this last section we compare the different forms of ALED against the beamformed MF. Table 6.1 delineates the parameters for the detector styles tested. Here, S is the number of soft decisions averaged and M is the number of symbols per channel in the equalizer.

Figure 6-14 displays the ROC curves for each detector listed in Table 6.1. It
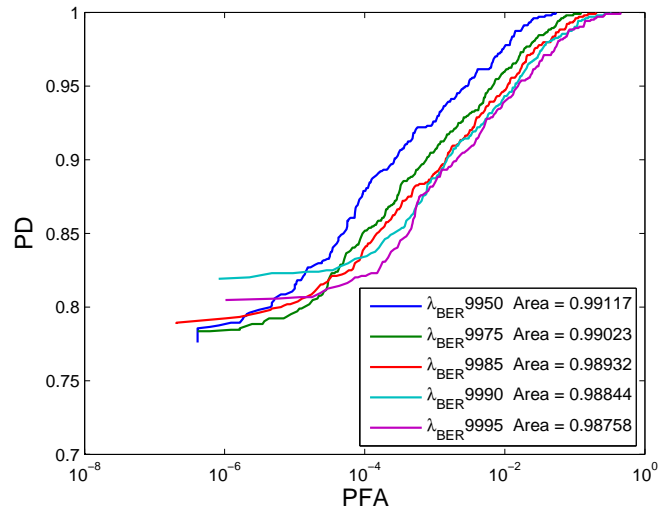
(a) 24X1 $M = 10$
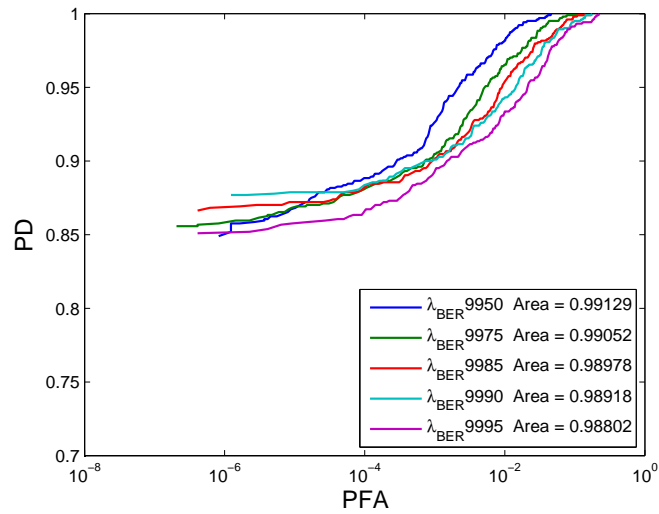
(b) 4X6 $M = 5$

Figure 6-13: Two ALED detectors (24X1 with $M = 10$ and 4X6 with $M = 5$) are compared with varying length BER averaging windows. The ROCs are ploted semilog due to the high performance of the ALED.

Detector Style	Parameters
ALED 24X1	$\lambda = 0.995$, $\lambda_{\mathrm{BER}} = 0.999$, $S = 25$, $M = 5, 10$
ALED 4X6	$\lambda = 0.998$, $\lambda_{\mathrm{BER}} = 0.999$, $S = 25$, $M = 5, 10$
ALED 1X24	$\lambda = 0.998$, $\lambda_{\mathrm{BER}} = 0.999$, $S = 25$, $M = 5$
MF	Beamformed to broadside, filter length $= 1778$ symbols

Table 6.1: Detector Parameters

is readily apparent that all forms of the ALED outperform the beamformed MF. However, out of the three styles of ALED, the 24X1 and 4X6 clearly outperform the 1X24.
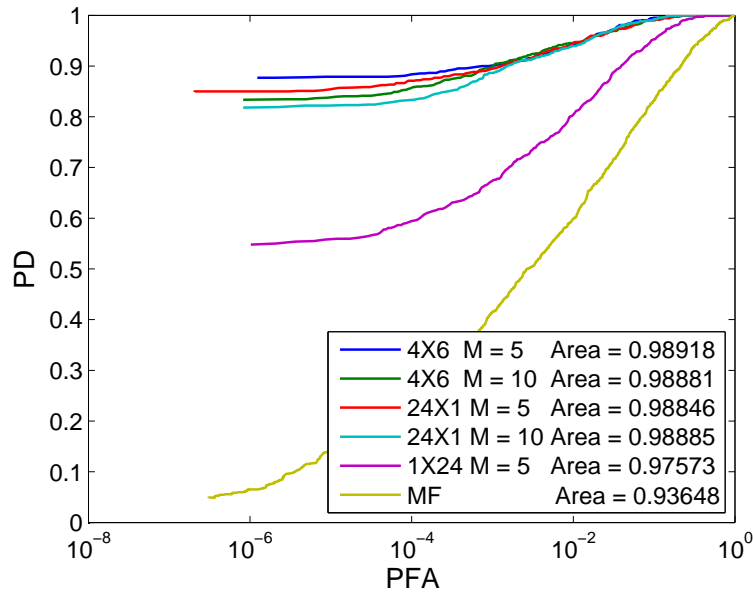

Figure 6-14: Five different versions of the ALED (parameters are given in Table 6.1) ROC curves are plotted against the broadside beamformed MF detector.

Chapter 7

Conclusions

7.1 Summary

This thesis examined methods of acoustic signal detection in a time varying ocean environment. In Chapter 2 we examined the energy detector as a method for detecting unknown signals. Its performance and constraints were evaluated and it was tested in simulation and on data from the KAM11 experiment. It was demonstrated that the ED had a low probability of detecting the acoustic signals transmitted during the KAM11 experiment when the SNR decreased to ~ -20 dB.

In Chapter 3 we derived the optimum detector for a known signal in white noise, the matched filter. Additionally we looked at the more common problem of a signal with an unknown complex amplitude in additive white Gaussian noise, again we arrived at the matched filter, but this time it was followed by an envelope detector. Losing knowledge about the signal hampered our ability to detect it. Chapter 3 also looked into different types of signals by way of the ambiguity function. The ambiguity function demonstrated how mismatch in estimated channel Doppler or sampling delay errors would reduce the peak output of the MF. The MF was tested in simulation and on data from the KAM11 experiment. The matched filter's performance was severely degraded over the theoretical MF. At our target SNR of -20 dB, for a $P_{\mathrm{D}} = 0.85$, a receiver would would be inundated with over 1000 false alarms per second.

In Chapter 4 we proposed the Adaptive Linear Equalizer Detector, and while a

rigorous mathematical derivation has not yet been completed, intuition on why this form of detector is desirable was given. Unlike the MF and ED, the ALED has many multi-channel forms and several different control variables. Each control variable was set based on an initial estimate of channel properties and then varied around this estimate to determine a region of optimum performance.

It was demonstrated that to achieve good performance, ALED's internal equalizers only need to span the main arrival of the signal. This was a desirable outcome because the majority of the computational work is dedicated to inverting the correlation matrix which is directly impacted by the length of the filter span. Additionally it was apparent that versions of the ALED that attempted to estimate larger portions of the correlation matrix required longer temporal averaging to reduce the noise.

Three different ALED structures were tested examining the two extremes in time-space correlation matrix estimates. The 24X1 only estimated the temporal correlation matrix for each channel and threw out the spatial correlations. The 1X24 attempted to estimate the entire matrix and the 4X6 was a compromise between the two. No mathematical derivation was given as to why one form may outperform the other and continued exploration into the area is needed. In our trial, the compromise of the 4X6 achieved the best performance for the 24 element array with our channel conditions.

An additional subtlety of the ALED detector that is beneficial in receiver design is in the nature of how the detection decision is made. In the MF, a detection is made based on the magnitude of the output of the filter. For a given signal to noise ratio, different threshold levels would be required for different ambient noise levels. Therefore as the environmental conditions change, the MF detector must be adjusted to maintain the same probability of false alarm. In the ALED, a detection is made based on a windowed BER. This BER is only dependent on the SNR, as the ambient noise increases and the SNR falls, the BER plateaus at approximately 50 percent. Therefore the ALED does not require the same constant adjustment to the detection threshold that the MF does.

Finally, the proposed ALED was compared to the MF on the KAM11 data. Its dramatic improvement over the MF demonstrated that signal detection and synchro-

nization at our target level of -20 dB SNR was achievable. The ALED achieved $P_\mathrm{D} = 0.85$ with a $P_\mathrm{FA} \leq 10^{-6}$. At our tested sampling rate of 12500 samples per second, this limits our false alarms to approximately one every 80 seconds. This results in five orders of magnitude improvement over the matched filter.

7.2 Future Work

We have shown an acoustic detector that takes the form of the ALED performs well in the time-varying ocean channel over a range of channel conditions. But no rigorous mathematical justification was given as to why the ALED should achieve such stellar performance, instead, intuition was substituted for this justification. Future study is required to determine why a detector of this form can outperform its matched filter counterpart.

Three styles of ALED were tested: 24X1, 4X6, and the 1X24, each attempting to estimate sections of, or the entire, time-space correlation matrix. The 4X6 outperformed both of the other detectors by discarding some of the spatial correlations but not all. Further study is required to determine what portions of the correlation matrix are required to make the best filter estimate. This area of research is not just limited to the ALED but would be beneficial in understanding ways to optimize all forms of linear adaptive equalization.

In this thesis the ALED was tested for a fixed source receiver range and only subject to the Doppler spread of the channel, not motion induced Doppler. A Doppler compensated ALED needs to be tested on moving platform transmissions to determine how its performance is effected.

Finally, in testing the ALED we painted with a broad brush and teased each of the input parameters in different directions trying to achieve optimum performance. We do not claim any one parameter is optimum, nor is complete mathematical justification given for why each specific value chosen. Additional study into how the ocean channel and structure of he signal effect parameter settings is required.

Bibliography

D. Brandwood, "A complex gradient operator and its application in adaptive array theory," *Microwaves, Optics and Antennas, IEE Proceedings H*, vol. 130, no. 1, pp. 11–16, 1983.

Y. Chan, B. Lee, R. Inkol, and F. Chan, "Detection of unknown signals by convolution," in *Communications, 2006 23rd Biennial Symposium on*, 0-0 2006, pp. 324 –327.

S. Haykin, *Adaptive Filter Theory*, 4th ed., ser. Prentice Hall Information and System Science Series, T. Kailath, Ed.   Prentice Hall, 2002.

J.-P. Hermand and W. Roderick, "Acoustic model-based matched filter processing for fading time-dispersive ocean channels: theory and experiment," *Oceanic Engineering, IEEE Journal of*, vol. 18, no. 4, pp. 447 –465, oct 1993.

W. Hodgkiss and J. Preisig, *Kauai Acomms MURI 2011 (KAM11) Experiment, Proc.11th European Conference on Underwater Acoustics (ECUA 2012), pp. 993-1000*, 2012.

W. Hodgkiss, H. Song, G. Deane, J. Preisig, M. Badiey, and A. Song, "Kauai acomms muri 2011 (kam11) experiment - trip report," July 2011.

F. B. Jensen, W. A. Kuperman, M. B. Porter, and H. Schmidt, *Computational ocean acoustics*, W. M. Hartmann, Ed.   Springer, 2011.

S. Kay, "Broadband detection of signals with unknown spectra," in *Acoustics, Speech, and Signal Processing, IEEE International Conference on ICASSP '85.*, vol. 10, apr 1985, pp. 1263 – 1265.

S. M. Kay, *Fundamentals of Statistical Signal Processing Volume II Detection Theory*, ser. Signal Processing Series, P. Hall, Ed.   Prentice Hall, 1998, vol. II.

E. Kelly, "An adaptive detection algorithm," *Aerospace and Electronic Systems, IEEE Transactions on*, vol. AES-22, no. 2, pp. 115 –127, march 1986.

D. North, "An analysis of the factors which determine signal noise discrimination in pulsed-carrier systems," *IEEE*, vol. 51, no. 7, pp. 1016–1027, 1963, this article is a reproduction of *North, D. O. (1943). "An analysis of the factors which determine*

signal/noise discrimination in pulsed carrier systems". RCA Labs., Princeton, NJ, Rep. PTR-6C.

A. V. Oppenheim and R. W. Schafer, *Discrete-Time Signal Processing*, 3rd ed. Prentice Hall, 2010.

A. V. Oppenheim and G. C. Verhese, "Signals, systems, and inference, class notes for 6.011: Introduction to communication, control and signal processing, massachusetts institute of technology," 2010.

A. Papoulis and S. U. Pillai, *Probability, Random Variables and Stochastic Processes*, 4th ed., M. Hill, Ed. McGraw Hill, 2002.

J. Proakis, *Digital Communications*, S. W. Director, Ed. McGraw Hill, 2000.

I. Reed, J. Mallett, and L. Brennan, "Rapid convergence rate in adaptive arrays," *Aerospace and Electronic Systems, IEEE Transactions on*, vol. AES-10, no. 6, pp. 853 –863, nov. 1974.

W. Remley, "Doppler dispersion effects in matched filter detection and resolution," *Proceedings of the IEEE*, vol. 54, no. 1, pp. 33 – 39, jan. 1966.

M. Stojanovic, "Recent advances in high-speed underwater acoustic communications," *Oceanic Engineering, IEEE Journal of*, vol. 21, no. 2, pp. 125 –136, apr 1996.

M. Stojanovic and J. Preisig, "Underwater acoustic communication channels: Propagation models and statistical characterization," *Communications Magazine, IEEE*, vol. 47, no. 1, pp. 84 –89, january 2009.

M. Stojanovic, J. Catipovic, and J. Proakis, "Phase-coherent digital communications for underwater acoustic channels," *Oceanic Engineering, IEEE Journal of*, vol. 19, no. 1, pp. 100 –111, jan 1994.

G. Turin, "An introduction to matched filters," *IEEE*, vol. 6, pp. 311–329, 1960.

H. Urkowitz, "Energy detection of unknown deterministic signals," *Proceedings of the IEEE*, vol. 55, no. 4, pp. 523 – 531, april 1967.

H. L. Van Trees, *Detection, Estimation, and Modulation Theory - Part lll - Radar-Sonar Processing and Gaussian Signals in Noise.* John Wiley & Sons, 2001.

L. Vergara, J. Moragues, J. Goslbez, and A. Salazar, "Detection of signals of unknown duration by multiple energy detectors," *Signal Processing*, vol. 90, no. 2, pp. 719 – 726, 2010. [Online]. Available: http://www.sciencedirect.com/science/article/pii/S0165168409003624

F. Wei, X. Xiaomei, Z. Lan, and C. Yougan, "A frame synchronization method for underwater acoustic communication on mobile platform," in *Image Analysis and Signal Processing (IASP), 2010 International Conference on*, april 2010, pp. 518 –522.